Hybrid chiral domain walls and skyrmions in magnetic multilayers

William Legrand, Jean-Yves Chauleau, Davide Maccariello, Nicolas Reyren, Sophie Collin, Karim Bouzehouane, Nicolas Jaouen, Vincent Cros, Albert Fert

To cite this version:

William Legrand, Jean-Yves Chauleau, Davide Maccariello, Nicolas Reyren, Sophie Collin, et al.. Hybrid chiral domain walls and skyrmions in magnetic multilayers. Science Advances , 2018, 4 (7), pp.eaat0415. 10.1126/sciadv.aat0415 . hal-02076573

HAL Id: hal-02076573
https://hal.science/hal-02076573v1

Submitted on 22 Mar 2019

PHYSICS

Hybrid chiral domain walls and skyrmions in magnetic multilayers

William Legrand[1], Jean-Yves Chauleau[1,2]*, Davide Maccariello[1], Nicolas Reyren[1], Sophie Collin[1], Karim Bouzehouane[1], Nicolas Jaouen[2], Vincent Cros[1†], Albert Fert[1]

Noncollinear spin textures in ferromagnetic ultrathin films are currently the subject of renewed interest since the discovery of the interfacial Dzyaloshinskii-Moriya interaction (DMI). This antisymmetric exchange interaction selects a given chirality for the spin textures and allows stabilizing configurations with nontrivial topology including chiral domain walls (DWs) and magnetic skyrmions. Moreover, it has many crucial consequences on the dynamical properties of these topological structures. In recent years, the study of noncollinear spin textures has been extended from single ultrathin layers to magnetic multilayers with broken inversion symmetry. This extension of the structures in the vertical dimension allows room temperature stability and very efficient current-induced motion for both Néel DWs and skyrmions. We show how, in these multilayered systems, the interlayer interactions can actually lead to hybrid chiral magnetization arrangements. The described thickness-dependent reorientation of DWs is experimentally confirmed by studying demagnetized multilayers through circular dichroism in x-ray resonant magnetic scattering. We also demonstrate a simple yet reliable method for determining the magnitude of the DMI from static domain measurements even in the presence of these hybrid chiral structures by taking into account the actual profile of the DWs. The existence of these novel hybrid chiral textures has far-reaching implications on how to stabilize and manipulate DWs, as well as skymionic structures in magnetic multilayers.

INTRODUCTION

The Dzyaloshinskii-Moriya interaction (DMI) is a form of antisymmetric exchange (*1*–*3*) that promotes canting between adjacent magnetic moments. As the DMI in ultrathin films originates from the strong spin-orbit coupling of interfacial atoms neighboring the magnetic layer (*4*, *5*), it is notably found in a ferromagnet (FM) interfaced with two different heavy metals, such as Pt/Co/Ir (*6*, *7*), or in magnetic layers inserted between a heavy metal and an oxide, such as Pt/CoFe/MgO (*8*, *9*). Because of the energy lowering of the Néel configuration [internal magnetization perpendicular to the domain wall (DW)] associated to the interfacial DMI, the demagnetizing effects inside the DW that usually favor the Bloch configuration (internal magnetization along the DW) can be overcome and the Néel orientation becomes favored (*10*). Depending on the types of interfacial atoms combined with the FM and on the stacking order, the DMI can also change sign, which determines whether clockwise (CW) or counterclockwise (CCW) chirality is preferred (*6*). This stabilization of chiral magnetic textures also helps to stabilize quasi-punctual solitonic structures called skyrmions, in the present case, Néel (hedgehog) skyrmions (*11*). To obtain stable and compact individual skyrmions at room temperature, a successful approach has been to stack up several repeats of an asymmetric combination of ultrathin layers (*7*, *12*). In this way, it is possible to stabilize columnar-shaped skyrmions, in which the increased magnetic volume reinforces their stability against thermal fluctuations up to room temperature, while still preserving both interfacial perpendicular magnetic anisotropy (PMA) in each ultrathin FM and required interfacial DMI due to the absence of inversion symmetry of the structure.

Here, our purpose is to investigate the actual thickness-dependent internal profile of chiral magnetic DWs and chiral skyrmions in Pt/Co/Ir- and Pt/Co/AlO_x-based multilayers with PMA. The studied multilayers are stackings made of 5 up to 20 repetitions of these trilayers with various magnetic layer thicknesses. Our study combines theoretical predictions, together with a direct experimental observation, of a vertical position–dependent reorientation of the chirality inside the magnetization texture in multilayers. By focusing first on the simplest case of DWs, we predict through micromagnetic simulations not only a significant variation of the DW width through the thickness of the multilayers but also, most importantly, a twisting of the internal DW texture along the thickness. In case of a large number of repetitions in the stacking, we find that topmost and bottommost layers host Néel orientations of opposite chiralities (CW and CCW), one in accordance with the chirality favored by the interfacial DMI and the other one being opposed to it. This reorientation thus results in an uncommon type of chiral composite Néel-Bloch DW. Then, we provide an experimental demonstration of the described reorientation of the DW texture in Pt/Co/AlO_x multilayers by directly observing the DW chirality close to the top surface through circular dichroism (CD) in x-ray resonant magnetic scattering (XRMS). These results involve reconsidering the common implicit assumption of a uniform magnetization through the thickness of the multilayers. With a better understanding of the actual depth profile of the DW structure through the thickness, we then describe a novel approach to measure the DMI in these multilayers using the experimentally measured size of parallel stripe domains. We next propose a simple model to predict the occurrence of DW twisting. We finally discuss how our findings open new opportunities to manipulate more efficiently this new type of composite chiral skyrmion in multilayers through a proper engineering of the interfacial spin-orbit torques (SOTs).

RESULTS

Dipolar field–induced reorientation of magnetic DWs

In ultrathin magnetic films, the interfacial DMI can be strong enough to stabilize chiral Néel DWs. Let us consider a single DW separating two perpendicularly magnetized domains of magnetization pointing

---

[1]Unité Mixte de Physique, CNRS, Thales, Univ. Paris-Sud, Université Paris-Saclay, Palaiseau 91767, France. [2]Synchrotron SOLEIL, L'Orme des Merisiers, Gif-sur-Yvette 91192, France.
*Present address: SPEC-UMR 3680 CEA-CNRS, 91191 Gif-sur-Yvette, France.
†Corresponding author. Email: vincent.cros@cnrs-thales.fr

down ($\mathbf{m} \cdot \mathbf{z} = -1$) for $x < 0$ and up ($\mathbf{m} \cdot \mathbf{z} = +1$) for $x > 0$. Denoting $\theta(x) = \arccos(\mathbf{m} \cdot \mathbf{z})$ the polar angle and ψ the (fixed) azimuthal angle of the magnetization inside the DW, the DW energy is given by (*13*)

$$\sigma_{\mathrm{dw}} = A\int_{-\infty}^{+\infty}\left(\frac{d\theta}{dx}\right)^2 dx + D\cos\psi\int_{-\infty}^{+\infty}\frac{d\theta}{dx}dx + K\int_{-\infty}^{+\infty}\sin^2\theta dx + \sigma_{\mathrm{dem}}(\psi) \tag{1}$$

where A is the Heisenberg exchange interaction amplitude, D is the interfacial DMI, K is the uniaxial anisotropy, and σ_{dem} is the demagnetizing energy associated to dipolar fields. Without DMI, the ψ dependence of σ_{dem} favors Bloch-type DWs ($\cos\psi = 0$). However, it is now well known that, in the presence of DMI, the energy of the DW can be lower for a Néel orientation ($\cos\psi = \pm 1$), which causes the reorientation of the internal magnetization of the DW and explains the stabilization of Néel structures (*5*, *8*, *14*). These Néel DWs in ultrathin films exhibit a fixed chirality controlled by the sign of the DMI and, notably, have proven to present extremely interesting current-driven dynamics (*10*).

In the recent years, the study of these chiral spin textures has become a very important research field both theoretically and experimentally. Most analyses of the spin configurations in single layers (for DWs and skyrmions) (*10*) assume a pure Néel profile and, for DWs, an energy independent of the DW spacing (uncoupled DWs). However, most often in multilayered stacks, the DWs are packed close to each other, meaning that the uncoupled DW approximation does not apply. Another complexity is that if the demagnetizing fields are strong (that is, for a large number of repetitions of magnetic layers), a DW structure between Bloch and Néel may arise ($0 < \psi < \pi/2$). These two effects have been recently considered by Lemesh *et al.* (*15*), who derived an analytical model of the demagnetizing energies for standard one-dimensional (1D) magnetization profiles. In this model, a classical DW profile with one free internal angle ψ is assumed, and the magnetic configuration is parameterized by Δ (DW width), λ (domain periodicity), and ψ only. Knowing the material parameters, a set of three nonlinear equations needs to be solved to get the equilibrium value of (Δ, λ, ψ). As we will demonstrate later, this model is very accurate for pure Néel DWs and allows us to estimate the value of D. It also allows us to a threshold minimum value of D that prevents internal tilting of the magnetization inside the DWs toward Bloch configuration.

This (Δ, λ, ψ) model is based on two strong assumptions: (i) The DW has a classical arctan profile without any x dependence for ψ, and (ii) all layers share the same DW profile, that is, without any z dependence. However, it is to be suspected that spin structures not uniform in the z direction can be stabilized in magnetic multilayers, as was suggested by micromagnetic simulations (*16*, *17*) and by imaging of the emergent field of skyrmions (*18*). We aim here to demonstrate that, in most of the multilayered material systems considered in recent experiments on skyrmions at room-temperature, the actual magnetization structure through the thickness of the multilayer is more complex. As a result of the competition between the different interactions, a novel type of chiral hybrid magnetic texture is stabilized with some serious consequences on their spin torque–driven dynamics.

To illustrate the consequences of the magnetic texture varying through the multilayers, we perform a series of micromagnetic simulations of the DW structure in a multilayer comprising 20 repetitions of X(1 nm)/Co(0.8 nm)/Z(1 nm), where X and Z are heavy metal or oxide nonmagnetic spacers, which is typical among multilayers and allows for stabilization of the skyrmions (*7*, *12*, *19*–*23*). We hence perform the micromagnetic simulation of the stripe domain configuration in the full geometry including all magnetic layers and nonmagnetic spacers (see Materials and Methods). To study the influence of the DMI on the DW configuration, we vary D to be −1.0, 0.0, 1.0, and 2.0 mJ m^{-2}, for each of which the DW configuration has been computed. The results of these simulations are compiled in Fig. 1, in which we present the evolution of the magnetization profile as a function of the layer position inside the stacking in three different ways. The first column displays cross-sectional views of the magnetization profile (Fig. 1, A to D), the second column displays the spread of polar (θ) angle of the DW magnetization across the DW in each layer (Fig. 1, E to H), and the third column displays the azimuthal (ψ) angle (Fig. 1, I to L). Each line of the figure then corresponds to the different DMI values. From these simulations, we find that, for a large range of DMI values, the DW internal magnetization is twisted between Néel and Bloch types along the direction (that is, the position of the magnetic layer in the stacking), leading to the formation of what we call a hybrid chiral DW structure.

One of the most striking results of these simulations is that the stabilized DW structures are not corresponding, whatever the value of D, neither to pure Bloch DWs ($\cos\psi = 0$), as usually expected for $D = 0$ in single layers (Fig. 1B), nor to pure Néel DWs ($\cos\psi = \pm 1$) even for D as large as 2.0 mJ m^{-2} (Fig. 1D). We further notice that, even for intermediate $D = \pm 1.0$ mJ m^{-2}(Fig. 1, A and C), the DWs do not exhibit an intermediate structure between Néel and Bloch types with a constant ψ angle of the magnetization inside the DW through the z direction but instead show a continuous variation of this ψ angle between all the magnetic layers of the stacking. These rather complex internal magnetization profiles, different from the single layer case, arise in these many-repeats multilayers from the competition between the interfacial DMI and the dipolar interactions between all layers. The resulting configuration can be described by the presence of a mostly Bloch ($\cos\psi$ close to zero) DW part in some of the intermediate magnetic layers, whereas the combined action of the demagnetizing fields and DMI fields leads to the stabilization of mostly Néel DW parts in the bottommost and topmost layers. The DW thus has opposite internal magnetization directions in the topmost and bottommost layers, that is, considered separately, topmost and bottommost layers have opposite chiralities. This kind of magnetic configuration was known in the absence of DMI for DWs (*24*, *25*) and bubbles (*26*) in magnetic thick layers. Here, we observe it for a large range of values of the DMI. We notice that the position of the Bloch DW part with respect to the central layer depends on the strength and sign of the DMI. For increasing $|D|$ values, the preference for a single chirality shifts more and more the position of the most Bloch DW (minimal $|\cos\psi|$) up or down, depending on the sign of D. For example, for $D = 2.0$ mJ m^{-2}, only the two topmost layers contain Néel-like DWs with a sense of rotation opposite to all others (for a large negative D, the two bottommost DWs will have an opposite rotation). Only for a large enough value of D ($|D| \geq 2.5$ mJ m^{-2} in the present case), the Bloch-like DWs are excluded, and the DW chirality is the same in all layers. The detailed description of the evolution of $\theta(x)$ and $\psi(x)$ profiles throughout the multilayer thickness is presented in section S1.

The discrepancy between the more elaborate micromagnetic simulations and the described analytical models stems from the absence, for the latter, of dependence of Δ and ψ along z. As described, we instead predict a twisted DW magnetization through the thickness, constituting a new kind of hybrid chiral DW in DMI systems. The complexity of the

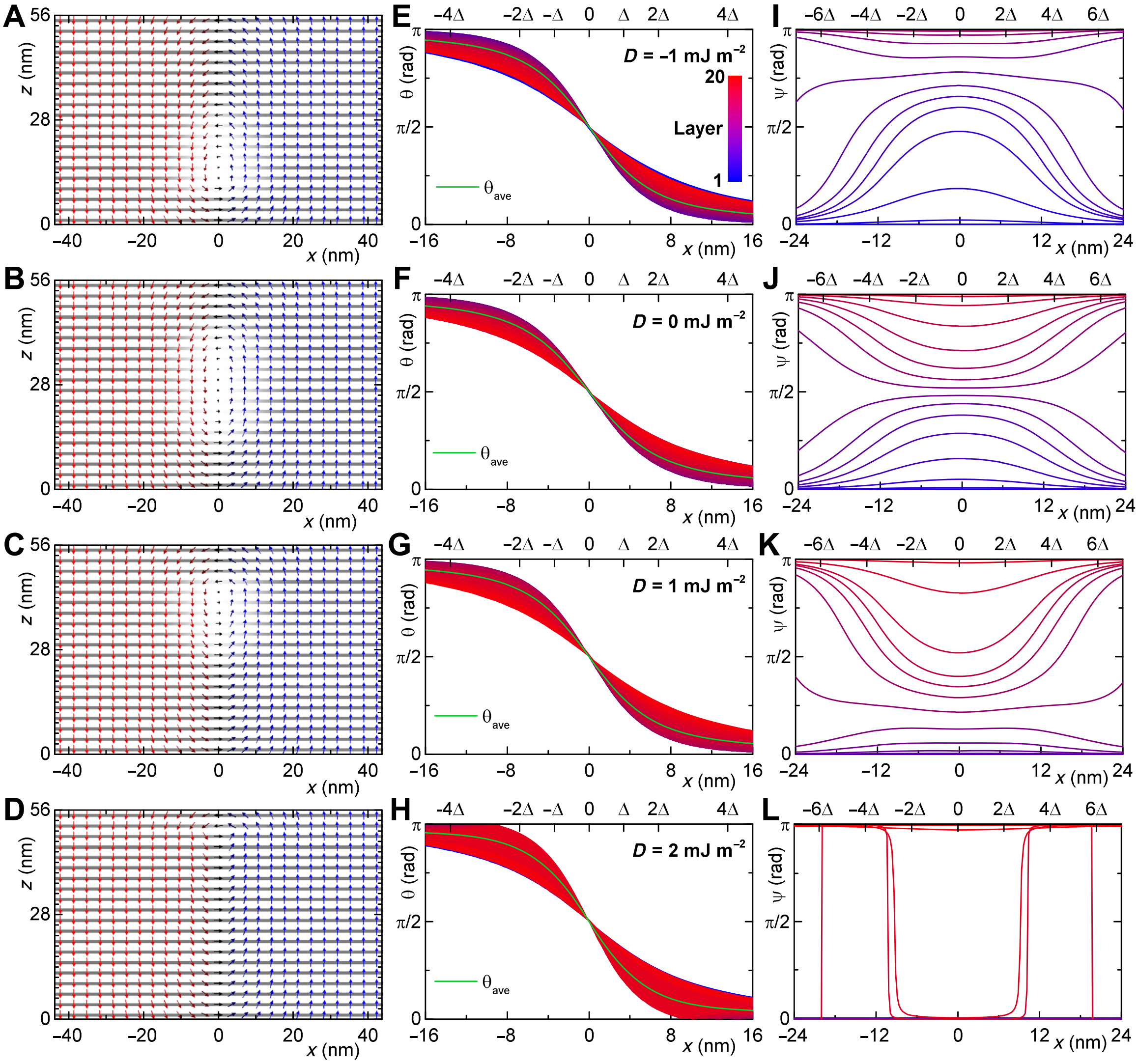

Fig. 1. Micromagnetic simulations of hybrid chiral DWs for different DMI values. (**A** to **D**) Cross-sectional view of a half simulation volume for $[X(1)/Co(0.8)/Z(1)]_{20}$ multilayer with $D = -1.0$, 0.0, 1.0, and 2.0 mJ m^{-2} (top to bottom); the gray lines correspond to the Co layers. Arrows point in the direction of the magnetization, m_z is given by the color of the arrows from red (−1) to blue (+1), while m_y is displayed by the color of the grid from black (−1) to white (+1). (**E** to **H**) Polar angle θ inside the DW in each layer for $D = -1.0$ to 2.0 mJ m^{-2}. The blue-to-red gradient filling corresponds to the envelop of θ of all profiles in the different layers from bottom to top [see color scale in (E)], while the green line is θ_{ave}, the averaged θ of all layers across the thickness. (**I** to **L**) Azimuthal angle ψ inside the DW in each layer for $D = -1.0$ to 2.0 mJ m^{-2}. The blue-to-red lines again correspond to the layers from bottom to top.

DW (or skyrmion, as will be seen later on) profiles in multilayers is well depicted in the curves shown in Fig. 1 (I to L).

The important difference of hybrid chiral DWs with previous models originates from the competition between the interlayer magnetostatic interactions and DMI, which results in these flux-closure DW configurations that never correspond to DWs with a fixed internal magnetization angle in between pure Bloch and Néel types. We will see later that, in our multilayers (but more generally in all the multilayered systems experimentally studied so far), the actual value (*27*) of D is inferior to 2.5 mJ m^{-2}, which is the threshold value that allows pure Néel DWs through all layers in the present case. In consequence, it becomes essential to consider that the actual DW (or skyrmion boundary) textures are similar to the ones that we just described. As detailed in the end of this study, this finding has profound implications for the spin torque–induced manipulation of these composite DWs (*28*) or skyrmions (*29*).

Direct observation of the internal twisting of the DWs

To experimentally verify the formation of the above-described composite DWs notably in the presence of a significant DMI, we grew several series of magnetic multilayered stackings by sputtering deposition (see Materials and Methods). The structures of the studied multilayers are reported in Table 1, starting from the substrate side //, where all thicknesses are given in nanometers and the numbers indexing the brackets are the number of repetitions of the base multilayer. The use of different buffer layers allows us to control the growth conditions and hence the amplitude of the magnetic anisotropy H_k and M_s values for similar stacks. The choice of opposite orders of the stackings allows us to get opposite signs of the DMI, while increasing the number of repetitions of the same trilayer base allows us to increase the influence of interlayer dipolar interactions.

To evidence the existence of the predicted DW twisting, we have measured the CD-XRMS, allowing us to directly probe the magnetization

Table 1. List of the studied magnetic multilayers investigated. The saturation magnetization M_s, the uniaxial anisotropy H_k, the measured domain periodicity, the estimated DW width, and the comparison of estimations of D with a fixed DW energy [K_{eff} model (*39*)], (Δ, λ, ψ) model, and the present full micromagnetic model are given for each multilayer. Two multilayers are not labeled as they have not been studied by CD-XRMS but only characterized by MFM to determine D with the different models.

No.	Multilayer stack	M_s (kA m^{-1})	H_k (mT)	λ (nm)	$\Delta_{\Delta,\lambda,\psi}$ (nm)	$D_{\sigma}K_{eff}$ (mJ m^{-2})	$D_{\Delta,\lambda,\psi}$ (mJ m^{-2})	D_{full} (mJ m^{-2})
I	//Pt 10/[**Ir 1/Co 0.6/Pt 1**]$_5$/Pt 3	840	330	167	7.27	−1.46	−1.43	−2.30
II	//Pt 10/[**Ir 1/Co 0.8/Pt 1**]$_5$/Pt 3	1229	640	150	4.13	−2.13	−2.00	−2.00
III	//Pt 11/[**Co 0.8/Ir 1/Pt 1**]$_5$/Pt 3	637	516	278	7.08	1.48	1.45	1.37
IV	//Ta 5/Pt 10/[**Co 0.8/Ir 1/Pt 1**]$_5$/Pt 3	683	748	488	5.77	1.69	1.64	1.63
V	//Pt 11/[**Co 0.8/Ir 1/Pt 1**]$_{10}$/Pt 3	637	516	244	6.03	1.53	1.50	1.52
VI	//Ta 5/Pt 10/[**Co 0.8/Ir 1/Pt 1**]$_{10}$/Pt 3	847	1088	250	4.11	2.11	2.08	2.06
VII	//Ta 15/Co 0.8/[**Pt 1/Ir 1/Co 0.8**]$_{10}$/Pt 3	957	500	256	5.00	−1.26	−1.21	−1.14
—	//Ta 10/Pt 7/[**Pt 1/Co 0.6/Al$_2$O$_3$ 1**]$_{20}$/Pt 3	1344	469	190	4.06	1.40	0.88	1.29
VIII	//Ta 10/Pt 7/[**Pt 1/Co 0.8/Al$_2$O$_3$ 1**]20/Pt 3	1373	358	175	3.72	1.20	1.20	1.01
—	//Ta 10/[**Al$_2$O$_3$ 1/Co 0.6/Pt 1/**]20/Pt 7	1120	332	131	4.79	−1.91	−1.93	−1.94
IX	//Ta 10/[**Al$_2$O$_3$ 1/Co 0.8/Pt 1/**]20/Pt 7	1245	228	131	4.33	−1.76	−1.78	−1.69

sense of rotation of the top layers of the stackings and thus the chirality of DWs as we recently demonstrated (*30*). For the present experiments, the energy is set at the L_3 Co edge, and the angle of incidence of the x-rays has been chosen to be 18.5°, corresponding to the first diffraction peak of the multilayer. Under these conditions, x-rays are mainly sensitive to the first 15 nm, which corresponds to only four to five repetitions from the top of the multilayered structure that predominate in the measured XRMS signal (see Materials and Methods). Before performing the XRMS experiments, all the samples have been demagnetized to reach a magnetic ground state composed of either labyrinthine alternating up and down magnetized domains or parallel stripe domains depending on the chosen demagnetization procedure (see Materials and Methods).

In Fig. 2 (A to C), we display the XRMS dichroism patterns (diffraction patterns with unpolarized x-rays are shown as insets) recorded for the multilayers labeled (II), (VII), and (IX) (with 5, 10, and 20 repetitions, respectively). These three multilayers are the ones having the Pt layer on top of the FM ($D < 0$; see Table 1). In the second line (see Fig. 2, D to F), the dichroism patterns are the ones obtained for the multilayers labeled (III), (V), and (VIII) (also with 5, 10, and 20 repetitions, respectively) that have the Pt layer below the FM ($D > 0$; see Table 1). Note that, for the first two columns, the multilayers have been demagnetized with an oscillating out-of-plane field, leading to a labyrinthine domain configuration that generates rings in the diffraction patterns. On the contrary, for multilayers (IX) and (VIII) shown in Fig. 2 (C and F), the demagnetization procedure was done by applying an oscillating in-plane field, leading to parallel stripe domain configuration and resulting in diffraction spots appearing on both sides of the specular peak. The corresponding magnetic force microscopy (MFM) images are shown in section S2.

Important conclusions can be drawn from this series of XRMS patterns. First, because the dichroic signal is, in all cases, maximum along the 90° to 270° axis, it can be concluded that all the DWs in these different multilayers share the same type of DW in surface, corresponding to Néel DWs as we demonstrated recently (*30*), instead of tilted DWs in between Néel and Bloch configurations. Second, we observe that, for all samples with Pt on top of the FM (Fig. 2, A to C), a positive (red color in our convention) dichroism at 90° is found. This means that the top few layers exhibit a CW Néel DW chirality whatever the number of repetitions in the multilayers, which is the DW configuration that can be expected for this sign of the DMI. On the opposite, for the first two multilayers with Pt below the FM (Fig. 2, D and E), the dichroic signal is reversed (maximum positive at 270°). It indicates an opposite, CCW Néel DW chirality for 5 and 10 repetitions, again as expected from the sign of the DMI. A striking observation is then that the dichroism pattern recorded for the 20-repeats multilayer with Pt below the FM (shown in Fig. 2F) is again positive at 90° and thus indicates a CW Néel chirality in surface, which is opposite to what is expected for a positive DMI–driven chirality. As we explained previously, this apparent discrepancy is a direct fingerprint of the competition between interlayer dipolar fields and DMI: Because of the 20 repeats in the multilayer, the impact of the dipolar fields is large enough to impose a reversal of the chirality of the DWs in the top layers. Note that we are able to observe this dipolar field–induced chirality reversal only for sample (VIII) and not for multilayer (IX), because for $D < 0$, the DMI field is opposite to the in-plane component of the dipolar field in the bottom layers (see the magnetic configurations in Fig. 1, A to D), which is not probed by CD-XRMS. On the contrary, for $D > 0$, the reversal of the top layers dominates the CD-XRMS signal. As a consequence, for sample (IX), the local DW chirality reversal occurs in the bottom layers, not probed by the x-rays in our XRMS configuration, and thus, the reorientation is not observed. The chirality reversal does not occur for the 5- and 10-repeats multilayers because the strength of the dipolar fields relative to the DMI fields in these multilayers is not strong enough, as will be shown later. These experimental results demonstrate the dipolar field–induced twisting of DWs in magnetic multilayers, as described in the previous section.

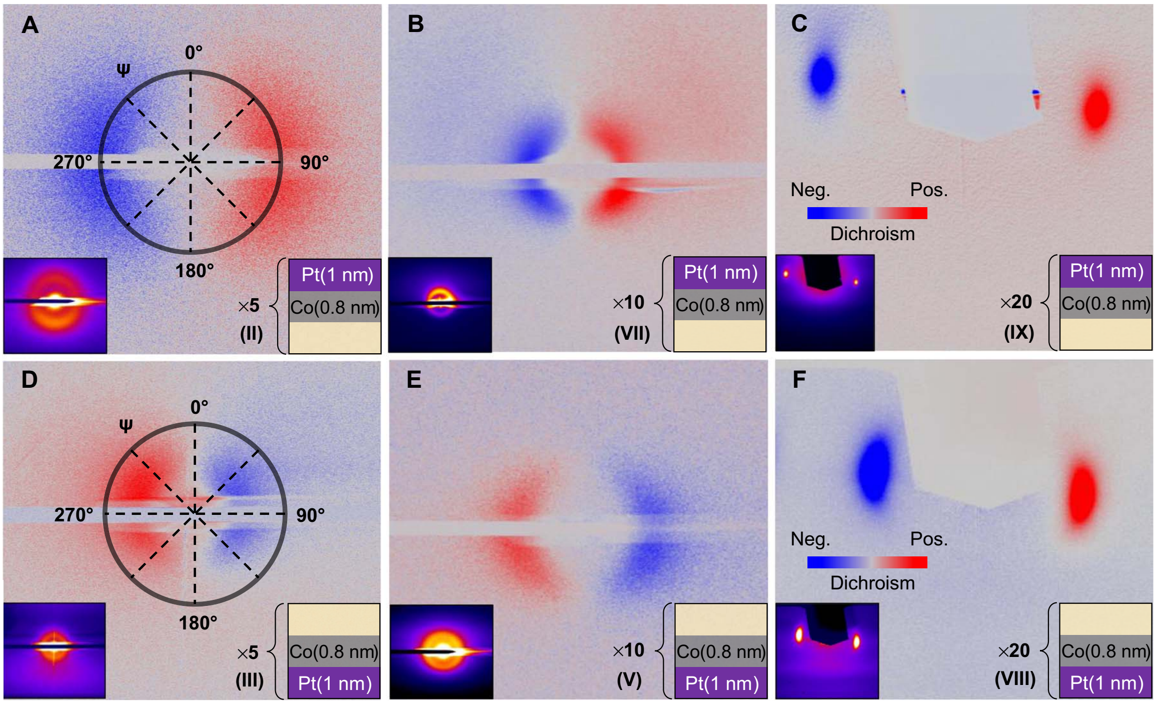

Fig. 2. CD-XRMS analysis of different multilayer stacking configurations. Multilayers with $D < 0$ and (**A**) 5 repetitions (sample II), (**B**) 10 repetitions (sample VII), and (**C**) 20 repetitions (sample IX) and with $D > 0$ and (**D**) 5 repetitions (sample III), (**E**) 10 repetitions (sample V), and (**F**) 20 repetitions (sample VIII). The dichroism is normalized for each image and indicated by the color scale from blue (negative) to red (positive). Left insets are the corresponding sum [circularly left (CL) + circularly right (CR)] images evidencing the magnetic distribution ordering. Right insets present schemes of the studied stackings.

Determination of *D* with hybrid chiral DW textures

Being able to get a quantitative estimation of the interfacial DMI amplitude has been the subject of numerous studies in the last couple of years because this parameter is crucial to understand and control both the statics and dynamics of chiral DWs and/or skyrmions. Different approaches have been proposed. In single magnetic layers, the interfacial DMI has been experimentally accessed using Brillouin light spectroscopy (BLS) (*27*, *31*), spin wave spectroscopy (*32*), chirality-induced asymmetric DW propagation (*9*, *33*), or asymmetric magnetization reversal (*34*–*36*). However, these different methods appear to be not reliable in the case of interfacial DMI in multilayered systems. A first reason is that dipolar fields and magnetic couplings between layers shall influence significantly the spin wave propagation and thus the analysis of BLS spectra. Moreover, because dense labyrinthic magnetic domains are formed at low fields, they thus prevent the observation of the asymmetric reversal needed to estimate the DMI. This is why, in multilayered systems, analysis of domain spacing in the demagnetized state or as a function of the perpendicular magnetic field has been proposed to estimate the magnitude of DMI (*7*, *12*, *37*). This approach is based on the fact that the DW periodicity λ is the result of the balance between domain demagnetization energy and DW energy (*38*), the latter being dependent on D, as described above. By measuring the DW periodicity λ in demagnetized multilayers (in our case, using XRMS or MFM; see Materials and Methods and acquired images in section S2), it is possible to determine D.

We show here how the existence of hybrid chiral DWs induced by dipolar fields has a large impact on the evaluation of D in multilayers. To get an accurate estimation even in the presence of the hybrid chiral DW structures that we identified, our procedure is then to rely on the micromagnetic simulations with the complete geometry, as exemplified above. We consider samples with the parallel stripe domains, and we vary the domain period in the simulation by changing the number of cells around the measured domain periodicity λ and then relax the system for different values of D. The extracted value D_{full} is D for which the energy density of the simulated system is minimum at λ (see section S3). The extracted D values for the different multilayers are listed in Table 1, in which we also compare D_{full} with the values of D estimated with the K_{eff} (*39*) and (Δ, λ, ψ) (*15*) models (see section S3). Although all models give consistent values for pure Néel DWs, we note significant differences as soon as at least one layer has a reversed chirality.

We emphasize that the measurement of the domain periodicity λ is error-free from the size of the MFM imaging probe (*40*) and that the sensitivity to local defects is reduced because of the averaging effect of imaging over sample areas much larger than λ. Thus, we believe that the most straightforward means to quantify the DMI in multilayers remains so far to find it from the measurement of λ in the ground state. Finally, another interesting aspect of this approach using the periodicity of stripe domains is that aligning parallel stripe domains with varying directions allows measurement of the DMI along different directions, which can give information about the anisotropy of DMI in materials having a crystalline structure that allows different DMI vectors along their different crystalline axes. We did not find anisotropic DMI in our samples.

Criterion for dipolar field–induced twisting of DW chirality

In the following, our objective is to establish a simple criterion describing the occurrence of twisted chiral DWs in magnetic multilayered systems. Considering the simplified case of parallel domains where DWs in all layers are Néel, we can study the stability of this pure Néel configuration. To this aim, we find under these assumptions the horizontal components of the dipolar- and DMI-induced fields inside the top layer for $D > 0$. We then compare the magnitude of the average action of both these fields on the DW profile, $\mathcal{A}_{\text{dip}}$ and $\mathcal{A}_{\text{DMI}}$, over the total width of the DW (see section S4 for the details of the calculations). As an example, we show the deduced field profiles (green and blue lines for DMI fields and interlayer dipolar interaction fields, respectively, right scale) for our multilayer (III) $[\text{Pt}(1)/\text{Co}(0.8)/\text{Ir}(1)]_5$ in Fig. 3, together with the DW horizontal magnetization component $m_x(x)$ profile (black curve, left scale). The dipolar interaction field B_{dip} (solid blue line) is obtained by summing surface (dashed blue line) and volume (dotted blue line) magnetic charge contributions. The small difference between the total field $B_{\text{dip,t}}$ and the dipolar interaction field with the other layers $B_{\text{dip}} = B_{\text{dip,s}} + B_{\text{dip,v}}$ comes from the horizontal component of the self-demagnetizing field of the top layer itself, which has no influence on the reorientation and which we do not include in the comparison of field actions. These analytically calculated field and magnetization profiles match the ones obtained from micromagnetic simulations (shown as squares of the corresponding colors in Fig. 3) under the assumptions mentioned just above.

When $|\mathcal{A}_{\text{dip}}| > |\mathcal{A}_{\text{DMI}}|$, for $D > 0$ ($D < 0$), the top layer (bottom layer) in-plane component of the magnetization inside the DW will reverse because of dipolar fields, so that a pure Néel DW throughout the whole stack is definitively not stable, whereas, for $|\mathcal{A}_{\text{dip}}| < |\mathcal{A}_{\text{DMI}}|$, Néel DWs of the same chirality can be stabilized in all layers. We can thus predict whether the DWs will reorientate or not, as shown in Fig. 4. The areas filled with a uniform color correspond to $|\mathcal{A}_{\text{dip}}| < |\mathcal{A}_{\text{DMI}}|$ in which case pure Néel-like DWs are stabilized. The color indicates the preferred DW chirality imposed by the DMI. When this condition is not fulfilled, that is, $|\mathcal{A}_{\text{dip}}| > |\mathcal{A}_{\text{DMI}}|$, corresponding to the gradient areas, the DW reorientation into flux-closure DWs leading to the stabilization of hybrid chiral DWs shall occur. The twisting is more and more pronounced when $|\mathcal{A}_{\text{dip}}|$ becomes stronger relative to $|\mathcal{A}_{\text{DMI}}|$, which is signified by the progressively lighter background color. To compare these predictions with our experiments, we also include in Fig. 4 the experimental observation of the DW chirality of the top layers determined by CD-XRMS in all our different multilayers. The colors of the squares labeled (I) to (IX) indicate the top-surface DW sense of rotation, blue corresponding to CCW and red corresponding to CW chiralities. As described above, the DW surface chirality for multilayer (VIII) is found in agreement with the prediction, that is, the corresponding square is red in a blue gradient area, meaning that the observed chirality is CW, due to dipolar fields, whereas the DMI favors a CCW chirality. We further notice that, for multilayers (VII) and (IX), the DW reorientation that shall occur in the bottom layers is not observed by our enhanced surface-sensitive technique. This can be seen in Fig. 4, as the corresponding squares are red in a red gradient area. We believe that these predictions are important as they allow us to easily obtain for a given set of magnetic parameters M_s, K_u, A, and multilayer geometry, an approximation of the threshold DMI value D_u that ensures a unique DW or skyrmion chirality inside the whole stacking. We will see in the last section that knowing whether twisting of the magnetization chirality occurs or not is crucial as the DW or skyrmion dynamics are strongly modified depending on their actual spin textures.

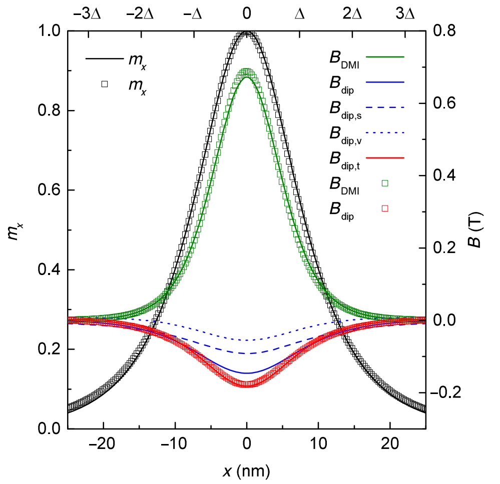

Fig. 3. DW profile (black, left scale) and analytical model for estimation of DMI (green, right scale) and dipolar (red, right scale) fields for the top layer of (III) $[\text{Pt}(1)/\text{Co}(0.8)/\text{Ir}(1)]_5$. The squares are the result of micromagnetic minimization of the energy, while the lines are the fields obtained from the model. The dashed and dotted blue lines are, respectively, surface and volume charge contributions to the interaction dipolar field (solid blue line). The red line is the total dipolar field from the model (obtained by adding the intralayer demagnetizing field to the interlayer interaction dipolar field). The parameter Δ has been adjusted for the magnetization arctan analytical profile to fit the micromagnetic profile.

Consequence on dynamics of skyrmions in multilayers

Stackings of ultrathin magnetic layers have been the subject of a large research effort recently for a demonstration of room temperature stabilization of small magnetic skyrmions. Moreover, it has already been shown (*12*, *21*, *41*, *42*) that the interfacial SOTs can be used to efficiently move these skyrmions. As aforementioned, the existence of a complex spin texture through the different magnetic layers of a stacking due to the competition between interlayer dipolar fields and DMI fields is not only expected for DWs (and observed as we have demonstrated here) but also should be equivalent for skyrmions in multilayers, as it has been also pointed out in other very recent works (*16*, *18*). Columnar skyrmions stabilized in multilayers, which is the favorite strategy to make them stable at room temperature, have a twisting of their chiral

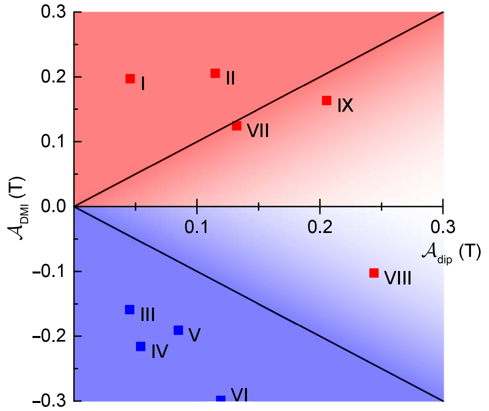

Fig. 4. Diagram comparing $\mathcal{A}_{\text{dip}}$ and $\mathcal{A}_{\text{DMI}}$ for each multilayer that has been characterized by CD-XRMS. When $|\mathcal{A}_{\text{dip}}| < |\mathcal{A}_{\text{DMI}}|$, pure Néel DWs are stabilized, and red (blue) indicates CW (CCW) chirality. The gradient areas correspond to $|\mathcal{A}_{\text{dip}}| > |\mathcal{A}_{\text{DMI}}|$ with more and more pronounced reorientation into flux-closure DWs. Colored squares indicate the chirality as it has been observed by CD-XRMS for each sample labeled by roman numbers, where red stands for CW chirality and blue stands for CCW chirality.

spin texture through their thickness that strongly alters their dynamics. However, to our knowledge, this crucial issue has never been properly addressed so far. We show in Fig. 5A an example of the actual skyrmion profile in a multilayer of structure $[X(1)/Co(1)/Z(1)]_{20}$ with $D = 0.8$ mJ m^{-2}, obtained by micromagnetic modeling similar as before (see Materials and Methods). Equivalent to what happens for DWs, the skyrmion profile exhibits a progressive reorientation from CCW Néel to Bloch through its thickness and finally to CW Néel chirality in the topmost magnetic layers. Moreover, the skyrmion diameter also evolves depending on the layer position in the stack, being larger in the central layers and smaller in the external layers. These skyrmions with Néel caps were recently predicted and thoroughly modeled by micromagnetic simulations for amorphous, 50-nm thick Gd/Fe layers (*16*). With our findings, we demonstrate that the stabilization of these hybrid chiral skyrmions occurs in multilayered stackings of ultrathin magnetic and nonmagnetic layers with strong interfacial DMI. In our multilayers, the different magnetic layers are exchange-decoupled because of Pt/Ir and Pt/Al_2O_3 spacers, which enhance reorientation effects as compared to exchange-coupled bulk materials such as Gd/Fe (*16*). In the following, we show that, through a precise engineering of the interfacial spin torques in stacked multilayers, new possibilities can be anticipated for achieving good control of the current-driven skyrmion dynamics.

To this aim, we have simulated the current-induced dynamics of isolated hybrid chiral skyrmions in an extended multilayer similar to the one shown in Fig. 5A for different values of the DMI and different spin injection geometries. Note that we only consider here damping-like torques originating from vertical spin currents, which can be provided, for example, by the spin Hall effect and a current flowing along the x direction. The resulting skyrmion velocities are reported in Fig. 5 (B to D). In Fig. 5B, we first present the case in which the torque is applied only in the first bottom and the first top layers and the injected spin polarization is opposite in these two layers. This can occur when the multilayer is enclosed between two layers of the same heavy metal. We find that both the longitudinal and transverse velocities remain constant for moderate values of D [with transverse velocity larger than longitudinal velocity, as it is already known, because of the gyrotropic motion of the topological skyrmions (*19*)] but then drop to zero when $|D| > D_u$, corresponding to the critical minimum value of D, above which skyrmions with a unique chirality across all layers are stabilized. The velocity drops because skyrmions of opposite chiralities are driven in opposite directions for identical polarizations of injected spins, but in the same direction for opposite spin injections. As a consequence, the driving forces on the bottom CCW and top CW Néel skyrmion layers add up in the range of D for which the chirality twist is present and cancel out for a uniform skyrmion chirality. In Fig. 5C, we present the results for the opposite case where the injected spins have identical polarizations in the bottommost and topmost layers, for example, with the multilayer enclosed between heavy metals of opposite spin Hall angles. In that case, we find that the skyrmion motion is completely canceled up to D_u because the hybrid complex spin texture leads to opposite skyrmion chiralities in bottommost and topmost layers. The motion occurs only for $|D| > D_u$, in which case top- and bottom-layer chiralities and injected spins are identical. Finally, for a uniform current

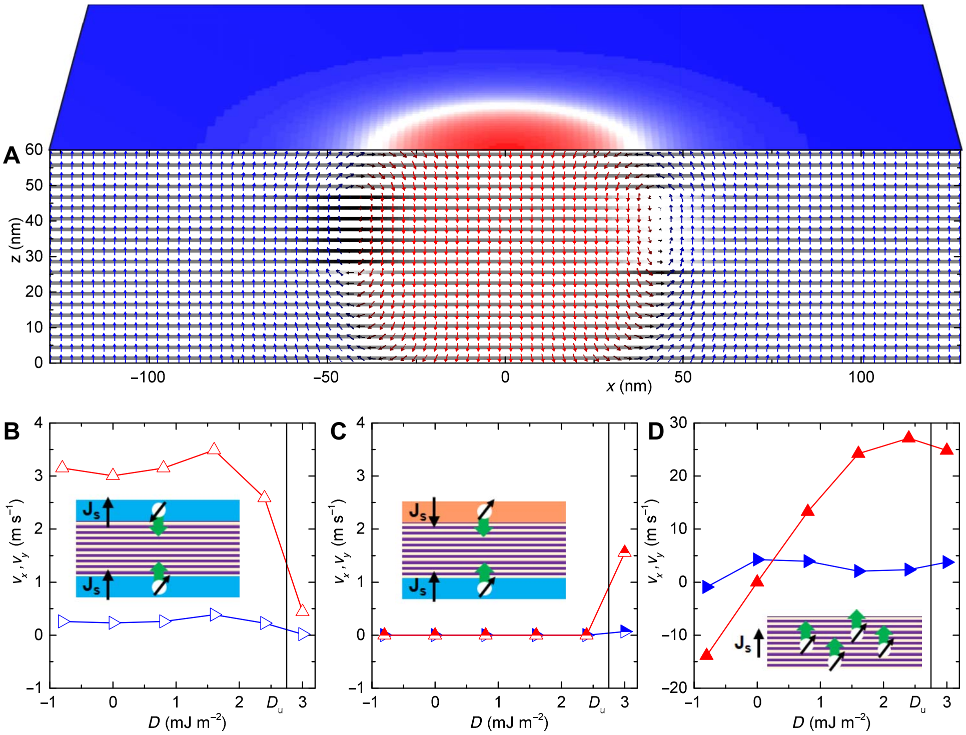

Fig. 5. Micromagnetic simulations of the dynamics of hybrid chiral skyrmions. (**A**) Cut view of the simulation volume for a $[X(1)/Co(1)/Z(1)]_{20}$ multilayer with $D = 0.8$ mJ m^{-2}. Arrows point in the direction of the magnetization, and m_z is given by the color of the arrows from red (−1) to blue (1), while m_y is displayed by the color of the grid from black (−1) to white (+1). The m_z component in the top layer is represented in perspective view by the color from red (−1) to blue (1). (**B** to **D**) Skyrmion velocities for different values of D and geometries. Right/up pointing blue/red triangles stand for horizontal/transverse velocity components, obtained for (B) opposite injection in bottommost/topmost layers, (C) identical injection in bottommost/topmost layers, and (D) uniform injection. The injection geometry is depicted by the inset in each case.

injection (for example, with a Pt layer adjacent to the bottom of each ferromagnetic layer; Fig. 5D), we find that the transverse (v_y) velocity is roughly proportional to D up to D_u (note the reduced velocity in cases of only external layer injection as compared to uniform injection within all layers, as fewer spins are injected in total). Again, it is because skyrmions of opposite chiralities are driven in opposite directions, which implies that the global motion is related to the balance of CCW and CW Néel skyrmion layers. Even if D does not directly affect the velocity of a given structure, as D controls the amount of layers with CCW and CW Néel orientations, it also controls the overall velocity. We also notice that, in this case, the driving forces compensate at $D = 0$, leading to a zero global v_y. The small v_x component arises from the Bloch part of the hybrid chiral skyrmion. The last case presented in Fig. 5D corresponds to the experimental studies of skyrmion dynamics reported by Woo *et al.* (*12*) and Litzius *et al.* (*20*) and provides a simple explanation why a very large (and hard to achieve) interfacial DMI is mandatory to achieve fast skyrmion motion in stacked multilayered systems in comparison to the case of single layers or multilayers with few repeats. In our multilayers, the intermediate Pt layers are thinner than the spin diffusion length. In this case the torques would be efficient only in the external layers, as is the case in Fig. 5B [multilayers (I) to (III), (V), and (VIII), enclosed between Pt layers] or in Fig. 5C [multilayers (IV), (VI) to (VII), and (IX), enclosed between Ta and Pt layers]. The high value of $D_u \approx 2.8$ mJ m^{-2} for 20 repetitions of X/Co(1 nm)/Z is above all reported values in multilayers. This shows that pure Néel skyrmions in these structures are very unlikely to occur. However, D_u can be lowered to realistic values in 20 repetitions of a thinner ferromagnetic layer such as in Pt/Co(0.6 nm)/AlO$_x$ or in structures for which M_s is lower. Finally, this series of simulations thus provides guidelines on how to design multilayers with many repetitions hosting skyrmions and how to engineer the interfacial spin torques to achieve a fast motion when hybrid chiral skyrmions are present in these multilayers.

DISCUSSION

The presented skyrmion dynamics simulations open new perspectives for the engineering of multilayered magnetic materials. Using these techniques, it will be possible to better control DW and skyrmion motion with SOTs in asymmetric multilayers and even in most common PMA symmetric stacks, such as Pt/Co and Pd/Co, which exhibit only low DMI or even no significant DMI. Notably, injecting spin Hall effect spin currents from the same material below and above the multilayer will lead to motion, as the chirality of the structure reverses from bottom to top. Moreover, as we have shown with the system displayed in Fig. 1, the balance between the number of layers and the value of D in the structure actually controls the position of the Bloch DW within the multilayer. It is thus possible to control the overall chirality of the structures by engineering the base multilayer repetition number, thus tuning the ratio of CCW Néel, Bloch, and CW Néel DWs. This would allow control of the direction of the motion in the case of a uniform spin current injection, as well as the chirality-related properties of DW and skyrmion motion. Moreover, our simulations of current-induced motion show the dynamical stability of the twisted chiral skyrmions as they are robust even under current injection, which can thus be used for spin current–induced motion.

With the help of our description, it is possible to understand and predict the occurrence of twisting of DW and skyrmion chiralities in multilayers. Notably, the common picture of a constant internal tilt inside the DW or constant chirality inside the skyrmion and through the different layers is revealed not to be valid. We have experimentally demonstrated this reorientation effect with a surface-sensitive x-ray diffraction technique, allowing us to observe the surface chirality of the DW configurations. These complex structures strongly modify the way the DMI should be quantified in magnetic multilayers. These results highlight the importance of advanced engineering of spin-orbit–related interfacial properties, combining PMA, SOT, and DMI in multilayered systems to promote the stabilization and the fast dynamics of ultrasmall skyrmions at room temperature, which are needed for many types of potential applications.

MATERIALS AND METHODS

Sample fabrication and characterization

All series of multilayers were grown by dc and radio frequency magnetron sputtering at room temperature on thermally oxidized silicon substrates, after deposition of a Ta or Pt buffer, as described in Table 1, and capped with Pt($\geq$3 nm) to prevent oxidation. We checked by x-ray reflectivity analysis that the quality of the interfaces in the multilayers is independent of the number of repetitions (up to 20). The saturation magnetization M_S and the effective perpendicular anisotropy field $H_{\mathrm{eff}} = H_K - M_S/2$ of each multilayer were obtained by SQUID (superconducting quantum interference device) and alternating gradient magnetometry measurements.

Demagnetization procedure and MFM imaging

We first compared the domain periodicity in the labyrinthine and aligned parallel domain configurations (obtained after out-of-plane and in-plane demagnetization procedures, respectively), measured by MFM (see the Supplementary Materials) in lift mode for our multilayer (VIII) [Pt(1)/Co(0.8)/AlO$_x$(1)]$_{20}$. For both in-plane and out-of plane demagnetization procedures, the maximum oscillating field was set higher than the anisotropy field in the multilayers, that is, $B \geq 1.2$ T. Then, the field was set to oscillate between positive and negative values with a decay factor of 0.5% until 0.5 mT was reached. For the in-plane demagnetization procedure, the multilayer was slightly tilted (~5°) with respect to the field to favor multiple reversals of the magnetization everywhere to get closer to a parallel stripe ground state. The extraction of the mean domain periodicity λ after Fourier transform revealed that it can differ significantly, by up to 20%, between the two demagnetization procedures. All rigorous models of magnetic domains in multilayers had, however, been derived for parallel stripe domains (*38*, *43*, *44*). Even if the difference in the domain width for the two demagnetized state configurations may be very small (*15*) in the ideal case, this deviation precluded the use of perpendicularly demagnetized domains for the estimation of the DMI, as only the values derived from the parallel stripe domains periodicity provided consistent results. The multilayers were imaged with Asylum Low Moment tips in a double-pass, tapping mode, followed by a lift mode at 20-nm height, at room temperature.

XRMS measurements

XRMS experiments were carried out at the SEXTANTS beamline of the SOLEIL synchrotron. The diffraction was measured under reflectivity conditions for CL and CR polarizations of the incident x-ray beam. The photon energy was set at Co L_3 edge (778.2 eV) using the RESOXS (resonant soft x-ray scattering) diffractometer. The diffracted x-rays were imaged on a square charge-coupled device (CCD) detector covering 6.1° at the working distance of this study. All the images were geometrically corrected along the Q_x direction to account for the projection effect related to the photon incidence angle of 18.5°. The sum of the images obtained with CL- and CR-polarized light gave rise to a diffraction pattern around the specular beam (which was blocked by a beamstop to avoid saturation of the CCD) in the reciprocal plane (Q_x,Q_y). Denoting I_{CL} and I_{CR} the intensities collected by the CCD for CL- and CR-polarized incident lights, the CD of the scattering signal is defined as $(I_{\mathrm{CL}} - I_{\mathrm{CR}})/(I_{\mathrm{CL}} + I_{\mathrm{CR}})$.

DW profiles—Micromagnetic simulations

To find the profiles of DWs in the stripe domain configuration without making assumptions on their shape, we performed micromagnetic simulations with the MuMax3 solver (*45*) in a 3D mesh accounting for the full geometry of the multilayers. The simulation volume was $\lambda \times 32$ nm $\times Np$, respectively, in the x, y, and z directions. Two DWs separating up, down, and up domains were initialized at $-\lambda/4$ and $\lambda/4$. Periodic boundary conditions inclusive of the periodic stray fields calculated for 64×64 identical neighbors in the x and y directions were introduced. The x cell size was 0.25 nm for the whole XRMS multilayer series. The z cell size was 0.2 nm, or 0.1 nm, when required by the values of layer spacing p and thickness t. Simulations were performed at 0 K.

Skyrmion velocities—Micromagnetic simulations

To find the potential current-induced velocities for different skyrmion chirality conditions and spin current geometries, we performed micromagnetic simulations in the full geometry for the multilayer $[\mathrm{X}(1)/\mathrm{Co}(1)/\mathrm{Z}(1)]_{20}$. Here, Co(1) was chosen to reduce the simulation grid size. The simulation volume was 256 nm × 256 nm × Np, respectively, in the x, y, and z directions. Periodic boundary conditions inclusive of the periodic stray fields calculated for 3×3 identical neighbors in the x and y directions were introduced. All cell sizes were 1 nm. Before current was applied, the configuration was relaxed from an initial Bloch skyrmion with CCW wall internal magnetization. The current density was then modeled as a fully polarized (along y) vertical spin current of current density $J = 2.5 \times 10^{10}$ A m^{-2}. The Gilbert damping α was set to 0.1, and the out-of-plane field was set to B = 200 or 300 mT (for $D > D_{\mathrm{u}}$). Because of this required increase of external field to confine the skyrmion to a stable circular shape for high $D > D_{\mathrm{u}}$, the skyrmion size was reduced and thus velocity as well (*19*), without affecting the discussed quantitative behavior. Simulations were performed at 0 K.

SUPPLEMENTARY MATERIALS

Supplementary material for this article is available at http://advances.sciencemag.org/cgi/content/full/4/7/eaat0415/DC1

Section S1. Detailed description of the hybrid chiral spin textures found in simulations

Section S2. Details of the determination of DMI with complete micromagnetic simulations

Section S3. MFM on the different samples

Section S4. Domain wall fields—Analytical derivation

Fig. S1. Detailed version of Fig. 1.

Fig. S2. MFM images of domain structures in studied multilayers.

REFERENCES AND NOTES

1. I. Dzyaloshinsky, A thermodynamic theory of "weak" ferromagnetism of antiferromagnetics. *J. Phys. Chem. Solids* **4**, 241–255 (1958).
2. T. Moriya, Anisotropic superexchange interaction and weak ferromagnetism. *Phys. Rev.* **120**, 91–98 (1960).
3. A. Fert, Magnetic and transport properties of metallic multilayers. *Mater. Sci. Forum* **59–60**, 439–480 (1990).
4. A. N. Bogdanov, U. K. Roßer, Chiral symmetry breaking in magnetic thin films and multilayers. *Phys. Rev. Lett.* **87**, 037203 (2001).
5. M. Bode, M. Heide, K. von Bergmann, P. Ferriani, S. Heinze, G. Bihlmayer, A. Kubetzka, O. Pietzsch, S. Blügel, R. Wiesendanger, Chiral magnetic order at surfaces driven by inversion asymmetry. *Nature* **447**, 190–193 (2007).
6. G. Chen, T. Ma, A. T. N'Diaye, H. Kwon, C. Won, Y. Wu, A. K. Schmid, Tailoring the chirality of magnetic domain walls by interface engineering. *Nat. Commun.* **4**, 2671 (2013).
7. C. Moreau-Luchaire, C. Moutafis, N. Reyren, J. Sampaio, C. A. F. Vaz, N. Van Horne, K. Bouzehouane, K. Garcia, C. Deranlot, P. Warnicke, P. Wohlhuter, J.-M. George, M. Weigand, J. Raabe, V. Cros, A. Fert, Additive interfacial chiral interaction in multilayers for stabilization of small individual skyrmions at room temperature. *Nat. Nanotechnol.* **11**, 444–448 (2016).
8. S. Emori, U. Bauer, S.-M. Ahn, E. Martinez, G. S. D. Beach, Current-driven dynamics of chiral ferromagnetic domain walls. *Nat. Mater.* **12**, 611–616 (2013).
9. S. Emori, E. Martinez, K.-J. Lee, H.-W. Lee, U. Bauer, S.-M. Ahn, P. Agrawal, D. C. Bono, G. S. D. Beach, Spin Hall torque magnetometry of Dzyaloshinskii domain walls. *Phys. Rev. B* **90**, 184427 (2014).
10. A. Thiaville, S. Rohart, E. Jué, V. Cros, A. Fert, Dynamics of Dzyaloshinskii domain walls in ultrathin magnetic films. *Europhys. Lett.* **100**, 57002 (2012).
11. N. Nagaosa, Y. Tokura, Topological properties and dynamics of magnetic skyrmions. *Nat. Nanotechnol.* **8**, 899–911 (2013).
12. S. Woo, K. Litzius, B. Krüger, M.-Y. Im, L. Caretta, K. Richter, M. Mann, A. Krone, R. M. Reeve, M. Weigand, P. Agrawal, I. Lemesh, M.-A. Mawass, P. Fischer, M. Kläui, G. S. D. Beach, Observation of room-temperature magnetic skyrmions and their current-driven dynamics in ultrathin metallic ferromagnets. *Nat. Mater.* **15**, 501–506 (2016).
13. M. Heide, G. Bihlmayer, S. Blügel, Dzyaloshinskii-Moriya interaction accounting for the orientation of magnetic domains in ultrathin films: Fe/W(110). *Phys. Rev. B* **78**, 140403 (2008).
14. S. Heinze, K. von Bergmann, M. Menzel, J. Brede, A. Kubetzka, R. Wiesendanger, G. Bihlmayer, S. Blügel, Spontaneous atomic-scale magnetic skyrmion lattice in two dimensions. *Nat. Phys.* **7**, 713–718 (2011).
15. I. Lemesh, F. Büttner, G. S. D. Beach, Accurate model of the stripe domain phase of perpendicularly magnetized multilayers. *Phys. Rev. B* **95**, 174423 (2017).
16. S. A. Montoya, S. Couture, J. J. Chess, J. C. T. Lee, N. Kent, D. Henze, S. K. Sinha, M.-Y. Im, S. D. Kevan, P. Fischer, B. J. McMorran, V. Lomakin, S. Roy, E. E. Fullerton, Tailoring magnetic energies to form dipole skyrmions and skyrmion lattices. *Phys. Rev. B* **95**, 024415 (2017).
17. C. Banerjee, P. Gruszecki, J. W. Klos, O. Hellwig, M. Krawczyk, A. Barman, Magnonic band structure in a Co/Pd stripe domain system investigated by Brillouin light scattering and micromagnetic simulations. *Phys. Rev. B* **96**, 024421 (2017).
18. Y. Dovzhenko, F. Casola, S. Schlotter, T. X. Zhou, F. Büttner, R. L. Walsworth, G. S. D. Beach, A. Yacoby, Magnetostatic twists in room-temperature skyrmions explored by nitrogen-vacancy center spin texture reconstruction; https://arxiv.org/pdf/1611.00673.pdf (2017).
19. W. Legrand, D. Maccariello, N. Reyren, K. Garcia, C. Moutafis, C. Moreau-Luchaire, S. Collin, K. Bouzehouane, V. Cros, A. Fert, Room-temperature current-induced generation and motion of sub-100 nm skyrmions. *Nano Lett.* **17**, 2703–2712 (2017).
20. K. Litzius, I. Lemesh, B. Krüger, P. Bassirian, L. Caretta, K. Richter, F. Büttner, K. Sato, O. A. Tretiakov, J. Förster, R. M. Reeve, M. Weigand, I. Bykova, H. Stoll, G. Schütz, G. S. D. Beach, M. Kläui, Skyrmion Hall effect revealed by direct time-resolved x-ray microscopy. *Nat. Phys.* **13**, 170–175 (2017).
21. S. Woo, K. M. Song, H.-S. Han, M.-S. Jung, M.-Y. Im, K.-S. Lee, K. S. Song, P. Fischer, J.-I. Hong, J. W. Choi, B.-C. Min, H. C. Koo, J. Chang, Spin-orbit torque-driven skyrmion dynamics revealed by time-resolved x-ray microscopy. *Nat. Commun.* **8**, 15573 (2017).
22. A. Soumyanarayanan, M. Raju, A. L. G. Oyarce, A. K. C. Tan, M.-Y. Im, A. P. Petrović, P. Ho, K. H. Khoo, M. Tran, C. K. Gan, F. Ernult, C. Panagopoulos, Tunable room-temperature magnetic skyrmions in Ir/Fe/Co/Pt multilayers. *Nat. Mater.* **16**, 898–904 (2017).
23. S. Jaiswal, K. Litzius, I. Lemesh, F. Büttner, S. Finizio, J. Raabe, M. Weigand, K. Lee, J. Langer, B. Ocker, G. Jakob, G. S. D. Beach, M. Kläui, Investigation of the Dzyaloshinskii-Moriya interaction and room temperature skyrmions in W/CoFeB/MgO thin films and microwires. *Appl. Phys. Lett.* **111**, 022409 (2017).
24. M. Labrune, L. Belliard, Stripe domains in multilayers: Micromagnetic simulations. *Phys. Status Solidi A* **174**, 483–497 (1999).
25. A. Bellec, S. Rohart, M. Labrune, J. Miltat, A. Thiaville, Domain wall structure in magnetic bilayers with perpendicular anisotropy. *Europhys. Lett.* **91**, 17009 (2010).
26. C. Moutafis, S. Komineas, C. A. F. Vaz, J. A. C. Bland, P. Eames, Vortices in ferromagnetic elements with perpendicular anisotropy. *Phys. Rev. B* **74**, 214406 (2006).
27. M. Belmeguenai, J.-P. Adam, Y. Roussigné, S. Eimer, T. Devolder, J.-V. Kim, S. M. Cherif, A. Stashkevich, A. Thiaville, Interfacial Dzyaloshinskii-Moriya interaction in perpendicularly magnetized Pt/Co/AlO$_x$ ultrathin films measured by Brillouin light spectroscopy. *Phys. Rev. B* **91**, 180405(R) (2015).
28. A. V. Khvalkovskiy, V. Cros, D. Apalkov, V. Nikitin, M. Krounbi, K. A. Zvezdin, A. Anane, J. Grollier, A. Fert, Matching domain-wall configuration and spin-orbit torques for efficient domain-wall motion. *Phys. Rev. B* **87**, 020402(R) (2013).

29. J. Sampaio, V. Cros, S. Rohart, A. Thiaville, A. Fert, Nucleation, stability and current-induced motion of isolated magnetic skyrmions in nanostructures. *Nat. Nanotechnol.* **8**, 839–844 (2013).
30. J.-Y. Chauleau, W. Legrand, N. Reyren, D. Maccariello, S. Collin, H. Popescu, K. Bouzehouane, V. Cros, N. Jaouen, A. Fert, Chirality in magnetic multilayers probed by the symmetry and the amplitude of dichroism in x-ray resonant magnetic scattering. *Phys. Rev. Lett.* **120**, 037202 (2018).
31. K. Di, V. L. Zhang, H. S. Lim, S. C. Ng, M. H. Kuok, J. Yu, J. Yoon, X. Qiu, H. Yang, Direct observation of the Dzyaloshinskii-Moriya interaction in a Pt/Co/Ni film. *Phys. Rev. Lett.* **114**, 047201 (2015).
32. J. M. Lee, C. Jang, B.-C. Min, S.-W. Lee, K.-J. Lee, J. Chang, All-electrical measurement of interfacial Dzyaloshinskii-Moriya interaction using collective spin-wave dynamics. *Nano Lett.* **16**, 62–67 (2016).
33. A. Hrabec, N. A. Porter, A. Wells, M. J. Benitez, G. Burnell, S. McVitie, D. McGrouther, T. A. Moore, C. H. Marrows, Measuring and tailoring the Dzyaloshinskii-Moriya interaction in perpendicularly magnetized thin films. *Phys. Rev. B* **90**, 020402(R) (2014).
34. S. Pizzini, J. Vogel, S. Rohart, L. D. Buda-Prejbeanu, E. Jué, O. Boulle, I. M. Miron, C. K. Safeer, S. Auret, G. Gaudin, A. Thiaville, Chirality-induced asymmetric magnetic nucleation in Pt/Co/AlO$_x$ ultrathin microstructures. *Phys. Rev. Lett.* **113**, 047203 (2014).
35. D.-S. Han, N.-H. Kim, J.-S. Kim, Y. Yin, J.-W. Koo, J. Cho, S. Lee, M. Klaui, H. J. M. Swagten, B. Koopmans, C.-Y. You, Asymmetric hysteresis for probing Dzyaloshinskii-Moriya interaction. *Nano Lett.* **16**, 4438–4446 (2016).
36. S. Kim, P.-H. Jang, D.-H. Kim, M. Ishibashi, T. Taniguchi, T. Moriyama, K.-J. Kim, K.-J. Lee, T. Ono, Magnetic droplet nucleation with a homochiral Néel domain wall. *Phys. Rev. B* **95**, 220402(R) (2017).
37. G. Yu, P. Upadhyaya, X. Li, W. Li, S. K. Kim, Y. Fan, K. L. Wong, Y. Tserkovnyak, P. K. Amiri, K. L. Wang, Room-temperature creation and spin-orbit torque manipulation of skyrmions in thin films with engineered asymmetry. *Nano Lett.* **16**, 1981–1988 (2016).
38. C. Kooy, U. Enz, Experimental and theoretical study of the domain configuration in thin layers of BaFe$_{12}$O$_{19}$. *Philips Res. Rep.* **15**, 7–29 (1960).
39. A. Mougin, M. Cormier, J. P. Adam, P. J. Metaxas, J. Ferré, Domain wall mobility, stability and Walker breakdown in magnetic nanowires. *Europhys. Lett.* **78**, 57007 (2007).
40. M. Baćani, M. A. Marioni, J. Schwenk, H. J. Hug, How to measure the local Dzyaloshinskii-Moriya interaction in skyrmion thin-films multilayers. https://arxiv.org/abs/1609.01615 (2016).
41. A. Hrabec, J. Sampaio, M. Belmeguenai, I. Gross, R. Weil, S. M. Chérif, A. Stashkevich, V. Jacques, A. Thiaville, S. Rohart, Current-induced skyrmion generation and dynamics in symmetric bilayers. *Nat. Commun.* **8**, 15765 (2017).
42. G. Yu, P. Upadhyaya, Q. Shao, H. Wu, G. Yin, X. Li, C. He, W. Jiang, X. Han, P. K. Amiri, K. L. Wang, Room-temperature skyrmion shift device for memory application. *Nano Lett.* **17**, 261–268 (2017).
43. H. J. G. Draaisma, W. J. M. de Jonge, Magnetization curves of Pd/Co multilayers with perpendicular anisotropy. *J. Appl. Phys.* **62**, 3318–3322 (1987).
44. B. Kaplan, G. A. Gehring, The domain structure in ultrathin magnetic films. *J. Magn. Magn. Mater.* **128**, 111–116 (1993).
45. A. Vansteenkiste, J. Leliaert, M. Dvornik, M. Helsen, F. Garcia-Sanchez, B. Van Waeyenberge, The design and verification of MuMax3. *AIP Adv.* **4**, 107133 (2014).

Acknowledgments: We acknowledge I. Lemesh and F. Büttner for sharing their manuscript (*15*) while it was still in press. **Funding:** Financial supports from FLAG-ERA SOgraph (ANR-15-GRFL-0005) and the European Union grant MAGicSky no. FET-Open-665095 are acknowledged. **Author contributions:** W.L., J.-Y.C., N.R., V.C., A.F., and N.J. conceived the project. W.L. deposited the multilayers with the help of S.C. W.L. performed the magnetic characterization and, together with D.M. and K.B., performed the MFM measurements of domain spacing. J.-Y.C., N.J., N.R., and V.C. performed the XRMS experiments. W.L. developed the analytical derivation part. W.L. and N.R. performed the micromagnetic simulations. All authors contributed to the analysis and interpretation of the experimental results and to the writing of the manuscript. **Competing interests:** The authors declare that they have no competing interests. **Data and materials availability:** All data needed to evaluate the conclusions in the paper are present in the paper and/or the Supplementary Materials. Additional data related to this paper may be requested from the authors.

Submitted 18 January 2018
Accepted 11 June 2018
Published 20 July 2018
10.1126/sciadv.aat0415

Citation: W. Legrand, J.-Y. Chauleau, D. Maccariello, N. Reyren, S. Collin, K. Bouzehouane, N. Jaouen, V. Cros, A. Fert, Hybrid chiral domain walls and skyrmions in magnetic multilayers. *Sci. Adv.* **4**, eaat0415 (2018).

Science Advances

Hybrid chiral domain walls and skyrmions in magnetic multilayers

William Legrand, Jean-Yves Chauleau, Davide Maccariello, Nicolas Reyren, Sophie Collin, Karim Bouzehouane, Nicolas Jaouen, Vincent Cros and Albert Fert

Sci Adv **4** (7), eaat0415.
DOI: 10.1126/sciadv.aat0415

Science Advances (ISSN 2375-2548) is published by the American Association for the Advancement of Science, 1200 New York Avenue NW, Washington, DC 20005.

Science Advances
AAAS

advances.sciencemag.org/cgi/content/full/4/7/eaat0415/DC1

Supplementary Materials for

Hybrid chiral domain walls and skyrmions in magnetic multilayers

William Legrand, Jean-Yves Chauleau, Davide Maccariello, Nicolas Reyren, Sophie Collin, Karim Bouzehouane, Nicolas Jaouen, Vincent Cros*, Albert Fert

*Corresponding author. Email: vincent.cros@cnrs-thales.fr

Published 20 July 2018, *Sci. Adv.* **4**, eaat0415 (2018)
DOI: 10.1126/sciadv.aat0415

This PDF file includes:

Section S1. Detailed description of the hybrid chiral spin textures found in simulations
Section S2. Details of the determination of DMI with complete micromagnetic simulations
Section S3. MFM on the different samples
Section S4. Domain wall fields—Analytical derivation
Fig. S1. Detailed version of Fig. 1.
Fig. S2. MFM images of domain structures in studied multilayers.

Section S1. Detailed description of the hybrid chiral spin textures found in simulations

We proceed here with a more detailed description of the results shown in Fig. 1 of the main text, in order to highlight some noticeable features of the hybrid chiral DWs. We noticed that (a) the DW width varies through the multilayer thickness ; (b) the z component of the DW magnetisation m_z cannot be simply assumed to follow an arctan function in all layers and none of the usual models allow to fit correctly the DW magnetisation structure.

Regarding point (a), we reproduce here in Fig. S1 the different representations of the DW profile from Fig. 1 in the main text, with the detailed layer by layer $\theta(x)$ profiles: as can be seen from the $\theta(x)$ profiles of Figs. 1e–h, the DW width varies significantly among the different layers. Again due to dipolar effects, the central, Bloch wall part is more compact than the Néel wall parts at top and bottom which extend over a larger width. Overall, the DW widths in the different layers vary significantly, by more than a factor of 2, as can be seen from the slopes at the center of the $\theta(x)$ profiles.

Regarding point (b), we find that in any individual layer of the stack, the DW profile cannot be properly described by the classical models. On the graphs of Figs. 1e–h, we add the average over all layers of the $\theta(x)$ profile of the micromagnetic model (orange lines), the DW profile (uniform along z) predicted by the so-called K_{eff} model (black lines), a model in which the multilayer is treated as an effective magnetic media and the DWs as non-interacting (see Methods for details), and the DW profile (also uniform along z) predicted by the (Δ,λ,ψ) model (*15*) (green lines). It can be clearly seen that the two latter profiles fail to reproduce both the exact shape of the DW, notably in the region of the tail, as well as the DW width. Notably, this difference demonstrates that the actual DW shapes are different from the commonly used arctan profile. Moreover, as can be seen from the strongly x dependent $\psi(x)$ profiles in Figs. 1i–l, the Bloch-Néel character of the DW in each layer varies across the DW (along x), instead of being fixed. As a consequence of the DW being partially Bloch, and only in the intermediate layers (combined x and z dependence of ψ), with varying DW widths, the average transverse magnetisation of the DWs is altered and DW energies turn to be significantly different from any simple model predictions. We note that when D exceeds $2.5\,\mathrm{mJ\,m^{-2}}$, the DWs resemble pure Néel DWs, and classical models get accurate, with a good agreement between micromagnetic and classical models.

Section S2. Details of the determination of DMI with complete micromagnetic simulations

We describe in this section our method for determining the magnitude of the DMI even in the presence of hybrid chiral spin textures. We first remind how, in the usual case of homochiral DWs and assuming that the demagnetised state observed with MFM is very close to the state of minimum energy given parallel stripe domains, it is possible to determine the DW energy σ_{dw} and deduce a rough estimation of the DMI magnitude $|D|$ from the domain periodicity λ with the so-called K_{eff} model. For uncoupled, independent DWs, separating domains of size $\lambda/2$ much larger than the

DW width $\Delta = \sqrt{A/K}$, there exist two straightforward approximations for K and thus for the DW energy (*47*). For single and ultrathin layers (of thickness $t \ll \Delta$), the demagnetising fields favour in-plane magnetisation inside the DW so that the anisotropy affecting the DW is the effective perpendicular anisotropy $K = K_u - \mu_0 M_s^2/2$. On the contrary, for thick layers ($t \gg \Delta$), the in-plane alignment inside the DW is disfavoured and $K = K_u + \mu_0 M_s^2/2$. However, these approximations cannot be applied in the intermediate thickness regime, which is the relevant case for magnetic multilayers such as the ones considered here, where both Δ and t are in the order of 10 nm. Following Ref. (*47*), we can refine the formula of the DW anisotropy K by assuming that for calculating demagnetising fields roughly, the DW can be considered as a monodomain magnetic body of width 2Δ, height t and infinite length. Due to the arctan profile of the DW, an elliptic shape is a good approximation. Inserting the demagnetising factors of the elliptic cylinder (*48*)

$$\begin{aligned} N_x &= \frac{t}{t+2\Delta} \\ N_z &= \frac{2\Delta}{t+2\Delta} \end{aligned}$$

in the effective anisotropy K gives a simple expression which allows to find the DW width by solving

$$\Delta = \sqrt{\frac{A}{K_u + \frac{\mu_0 M_s^2}{2}\frac{(t-2\Delta)}{(t+2\Delta)}}}$$

By summing the contributions of exchange, DMI, anisotropy and demagnetising fields in the elliptic body (*10*), the DW energy is then

$$\sigma_{\mathrm{dw}} = 2A/\Delta + 2K_u\Delta - \pi\left|D\right| + \frac{\mu_0 M_s^2}{2}2\Delta\left(\frac{t-2\Delta}{t+2\Delta}\right)$$

Concerning the demagnetising energy arising from the domains, in the zero width (as $\lambda \gg \Delta \sim 0$) model we get (*42*)

$$\epsilon_{\mathrm{demag}} = 2\mu_0 M_s^2 \frac{\lambda}{t} \frac{1}{\pi^3} \sum_{n \geqslant 1,\mathrm{odd}}^{\infty} \frac{1}{n^3} \left(1 - \mathrm{e}^{-2\pi n t/\lambda}\right)$$

which allows one to find σ_{dw} from the observed λ. Indeed, by minimising the total energy $\epsilon_{\mathrm{tot}} = 2\sigma_{\mathrm{dw}}/\lambda + \epsilon_{\mathrm{demag}}$ relative to λ we get

$$\sigma_{\mathrm{dw}} = \mu_0 M_s^2 \frac{\lambda^2}{t} \frac{1}{\pi^3} \sum_{n \geqslant 1,\ \mathrm{odd}}^{\infty} \frac{1}{n^3} \left(1 - \mathrm{e}^{-2\pi n t/\lambda} - \frac{2\pi n t}{\lambda} \mathrm{e}^{-2\pi n t/\lambda}\right)$$

which allows one to find D by equaling it to the previous expression of σ_{dw} as we know M_s, K_u, and A estimated to be $10\,\mathrm{pJ\,m^{-1}}$. A was obtained by determining the Curie temperature from temperature-dependent SQUID measurements. To apply this K_{eff} model, the multilayer is treated as an effective magnetic medium filled with diluted moments. Note that this assumption is valid as long as the periodicity of the stack is not significantly larger than the DW size (*15*), which is always verified for the samples considered here.

This characterisation method has led to the evidence of a significant DMI in magnetic multilayers with broken inversion symmetry (*7, 12*). It has however been pointed out recently that such measurements can be largely erroneous when neglecting stray-field effects on the DW size and spacing, so that a more comprehensive model is required for multilayers (*15*). When dipolar interactions become significant but the DW internal configuration remains uniform, a more detailed model such as the (Δ,λ,ψ) is more accurate (*15*). Nevertheless, we now suspect that complex DW or skyrmion structures can arise in magnetic multilayers depending of the relative strengths of dipolar interactions and DMI, which calls for a more careful analysis of their spin textures (*16*–*18*).

In order to find the strength of the DMI in the stripe domains configuration without making assumptions on the DW profiles, we performed micromagnetic simulations with the Mumax3 solver (*49*) in a 3D mesh accounting for the full geometry of the multilayers. The simulation volume is $\lambda \pm d\lambda \times 32\,\mathrm{nm} \times Np$, respectively, in the x, y and z directions. Two DWs separating up, down and up domains are initialised at $(-\lambda \pm d\lambda)/4$ and $(\lambda \pm d\lambda)/4$, which corresponds to the $\lambda \pm d\lambda$ periodicity of the stripes. Periodic boundary conditions inclusive of the periodic stray fields calculated for 64×64 identical neighbors in the x and y directions were introduced. The x cell size was 0.25 nm for the XRMS multilayers series. The z cell size was 0.2 nm, or 0.1 nm when required by the values of layer spacing p and thickness t. Simulations are performed at 0 K.

Given the experimental value of λ, the simulation is initialised with its DWs having a $\psi = 45°$ in-plane tilt of internal moments for x sizes $\lambda{-}2\,\mathrm{nm}$,$\lambda{-}1\,\mathrm{nm}$,λ,$\lambda{+}1\,\mathrm{nm}$,$\lambda{+}2\,\mathrm{nm}$. Each system is relaxed in order to find the ground state energy density $\epsilon(\lambda)$, so that we get the local value of $d\epsilon/d\lambda$ at λ. Performing this operation for various values of D allows to find D_{full} such that $d\epsilon/d\lambda = 0$ by interpolation.

Section S3. MFM on the different samples

We present here in Fig. S2 the Magnetic Force Microscopy (MFM) images of the demagnetised multilayers that have been used in order to extract the mean domain periodicity.

Section S4. Domain wall fields–Analytical derivation

We want here to derive an analytical formula descriminating DWs that will exhibit hybrid chirality. For this we consider the fields acting on the top layer for the case of $D > 0$ (which is equivalent to consider fields on the bottom layer for $D < 0$). In order to find the dipolar field in the top layer of the multilayer, we have to find the solution for the potential ϕ of Laplace equation $\nabla^2\phi = \rho_V$ with ρ_V the volume charges and boundary conditions related to surface charges ρ_S. As was done in Lemesh et al. (*15*) we separate volume and surface magnetic charges contributions. We consider λ-periodic stripe domains in the x direction (uniform along y) and approximate the DW profile by the arctan profile (which we know to be an approximation). We note t the magnetic layer thickness, p the multilayer periodicity and N the total number of layers. Assuming a perfectly Néel DW in all layers, we can obtain the DW width Δ from the (Δ,λ,ψ) model.

We first solve for a single layer $\nabla^2\phi = 0$ with $\partial\phi/\partial z(x, \pm t/2^-) = \partial\phi/\partial z(x, \pm t/2^+) \pm \rho_S(x)$. As $\rho_S(x)$ corresponds to the charges of two opposite, alternate DW profiles (up to down and down to up) localised every $\lambda/2$, we can write (*15*)

$$\rho_S(x) = \sum_{k=-\infty}^{\infty} f_S(x) * \delta(x - k\lambda) + \sum_{k-\infty}^{\infty} -f_S(x) * \delta(x - k\lambda - \lambda/2)$$

where f corresponds to a single DW profile $f_S(x) = M_s m_z(x) = M_s \tanh{(x/\Delta)}$, that is, by combining all Dirac functions and swapping the derivatives in the convolution product,

$$\rho_S(x) = \frac{f_S'(x)}{2} * g(x)$$

with

$$g(x) = \begin{cases} 1 & x \in [k\lambda; \lambda/2 + k\lambda[\\ \\ -1 & x \in [\lambda/2 + k\lambda; \lambda + k\lambda[\end{cases}$$

As the magnetic charge distribution is λ periodic we can decompose it in Fourier series

$$\rho_S(x) = \sum_{k=-\infty}^{\infty} \bar{\rho_S}(k) \mathrm{e}^{-\frac{2\pi k x}{\lambda}}$$

and solve

$$\nabla^2 \bar{\phi}(k,z) = \frac{\partial^2 \bar{\phi}(k,z)}{\partial z^2} - \left(\frac{2\pi k}{\lambda}\right)^2 \bar{\phi}(k,z) = 0$$

with $\partial\bar{\phi}/\partial z(k, \pm t/2^-) = \partial\bar{\phi}/\partial z(\pm t/2^+) \pm \bar{\rho_S}$. By properties of the Fourier transform defined as

$$\bar{f}(\xi) = \frac{1}{\sqrt{2\pi}} \int f(x) \mathrm{e}^{-i\xi x} dx$$

we know that

$$\bar{\rho_S} = \overline{f_S'/2 * g} = \sqrt{2\pi}\left(\overline{f_S'}\bar{g}\right)/2 = \sqrt{2\pi} i \xi \overline{f_S} \bar{g}/2$$

so that for positive integer k

$$\begin{aligned} \bar{\rho_S}(\frac{2\pi k}{\lambda}) &= \frac{\sqrt{2\pi} i \pi k}{\lambda}\left[-iM_s\Delta\sqrt{\frac{\pi}{2}}\,\mathrm{csch}\left(\frac{\pi^2\Delta k}{\lambda}\right)\right]\left[-\frac{4i}{\sqrt{2\pi}k}\sin^2\left(\frac{k\pi}{2}\right)\right] \\ &= -i\sqrt{\frac{\pi}{2}}\frac{4\pi M_s\Delta}{\lambda}\sin^2\left(\frac{k\pi}{2}\right)\mathrm{csch}\left(\frac{\pi^2\Delta k}{\lambda}\right) \end{aligned}$$

Using the boundary conditions to solve Laplace equation (*45*) above the layer we find for $z > t/2$

$$\phi(x,z) = \sum_{k=1}^{\infty} \frac{2M_s\Delta}{k}\sin^2\left(\frac{\pi k}{2}\right)\mathrm{csch}\left(\frac{\pi^2\Delta k}{\lambda}\right)\sinh\left(\frac{\pi k t}{\lambda}\right)\sin\left(\frac{2\pi k x}{\lambda}\right)\mathrm{e}^{-\frac{2\pi k z}{\lambda}}$$

with $x = 0$ in the center of the DW between down and up domains. For a multilayer there are N layers located at $p/2 + kp$ with $0 \leq k \leq N - 1$. In the top layer, the interlayer interaction field will then be the sum of all other layers stray fields

$$B_{\text{dip,S}}(x) = -\mu_0 \frac{\partial}{\partial x} \left[\sum_{n=1}^{N-1} \phi(x, np) \right]$$

that is by grouping the exponent sum

$$\begin{aligned} B_{\text{dip,S}}(x) &= -\mu_0 \frac{\partial}{\partial x} \left[\sum_{k=1,\text{odd}}^{\infty} \frac{2M_s\Delta}{k} \operatorname{csch}\left(\frac{\pi^2 \Delta k}{\lambda}\right) \sinh\left(\frac{\pi k t}{\lambda}\right) \sin\left(\frac{2\pi k x}{\lambda}\right) \frac{\mathrm{e}^{-\frac{2\pi k p}{\lambda}} - \mathrm{e}^{-\frac{2\pi k N p}{\lambda}}}{1 - \mathrm{e}^{-\frac{2\pi k p}{\lambda}}} \right] \\ &= -\mu_0 \sum_{k=1,\text{odd}}^{\infty} \frac{4\pi M_s \Delta}{\lambda} \operatorname{csch}\left(\frac{\pi^2 \Delta k}{\lambda}\right) \sinh\left(\frac{\pi k t}{\lambda}\right) \cos\left(\frac{2\pi k x}{\lambda}\right) \frac{\mathrm{e}^{-\frac{2\pi k p}{\lambda}} - \mathrm{e}^{-\frac{2\pi k N p}{\lambda}}}{1 - \mathrm{e}^{-\frac{2\pi k p}{\lambda}}} \end{aligned}$$

which can be determined numerically.

We can now solve for a single layer $\nabla^2 \phi = \rho_V(x)$ for $|z| < t/2$ and $\nabla^2 \phi = 0$ for $|z| > t/2$, with continuity of $\partial\phi/\partial z$ at $z = \pm t/2$. We have again

$$\rho_V(x) = \sum_{k=-\infty}^{\infty} f_V(x) * \delta(x - k\lambda) + \sum_{k-\infty}^{\infty} -f_V(x) * \delta(x - k\lambda - \lambda/2)$$

with

$$f_V(x) = -M_s \nabla \cdot \mathbf{m} = -M_s \frac{\partial m_x}{\partial x} = \frac{M_s}{\Delta} \frac{\tanh(x/\Delta)}{\cosh(x/\Delta)}$$

the volume charges for a single DW. Similar to ρ_S we get $\rho_V(x) = [f_V'(x) * g(x)]/2$ and for positive integer k,

$$\begin{aligned} \bar{\rho_V}\left(\frac{2\pi k}{\lambda}\right) &= \overline{f_V'/2 * g}(k) = \sqrt{2\pi} i \, (2\pi k/\lambda) \, \overline{f_V} \bar{g}/2 \\ &= \frac{\sqrt{2\pi} i \pi k}{\lambda} \left[i M_s \Delta \frac{2\pi k}{\lambda} \sqrt{\frac{\pi}{2}} \operatorname{sech}\left(\frac{\pi^2 \Delta k}{\lambda}\right) \right] \left[-\frac{4i}{\sqrt{2\pi} k} \sin^2\left(\frac{k\pi}{2}\right) \right] \\ &= -i \sqrt{\frac{\pi}{2}} \frac{-8\pi^2 M_s \Delta k}{\lambda^2} \operatorname{sech}\left(\frac{\pi^2 \Delta k}{\lambda}\right) \sin^2\left(\frac{k\pi}{2}\right) \end{aligned}$$

Using the boundary continuity to solve Laplace equation above the layer we find for $z > t/2$

$$\phi(x,z) = \sum_{k=1}^{\infty} \frac{2M_s\Delta}{k} \sin^2\left(\frac{\pi k}{2}\right) \operatorname{sech}\left(\frac{\pi^2\Delta k}{\lambda}\right) \sinh\left(\frac{\pi k t}{\lambda}\right) \sin\left(\frac{2\pi k x}{\lambda}\right) \mathrm{e}^{-\frac{2\pi k z}{\lambda}}$$

so that

$$B_{\text{dip,V}}(x) = -\mu_0 \sum_{k=1,\text{odd}}^{\infty} \frac{4\pi M_s\Delta}{\lambda} \operatorname{sech}\left(\frac{\pi^2\Delta k}{\lambda}\right) \sinh\left(\frac{\pi k t}{\lambda}\right) \cos\left(\frac{2\pi k x}{\lambda}\right) \frac{\mathrm{e}^{-\frac{2\pi k p}{\lambda}} - \mathrm{e}^{-\frac{2\pi k N p}{\lambda}}}{1 - \mathrm{e}^{-\frac{2\pi k p}{\lambda}}}$$

One still has to consider the self-demagnetising field of the top layer itself. The surface charges distribution does not contribute to the z-average of the field as it generates a field antisymmetric in z. However the volume charges contribution must be considered. Solving again the Laplace equation but inside the magnetic layer ($|z| < t/2$) we find

$$B_{\text{dip}}(x,z) = \mu_0 \sum_{k=1,\text{odd}}^{\infty} \frac{4\pi M_s\Delta}{\lambda} \operatorname{sech}\left(\frac{\pi^2\Delta k}{\lambda}\right) \cos\left(\frac{2\pi k x}{\lambda}\right) \left[\cosh\left(\frac{2\pi k z}{\lambda}\right) \mathrm{e}^{\frac{\pi k t}{\lambda}} - 1\right]$$

that we can average between $z = -t/2$ and $z = t/2$ to obtain the horizontal component of the self-interaction field of the top layer

$$B_{\text{dip,self}}(x) = \mu_0 \sum_{k=1,\text{odd}}^{\infty} \frac{4\pi M_s\Delta}{\lambda} \operatorname{sech}\left(\frac{\pi^2\Delta k}{\lambda}\right) \cos\left(\frac{2\pi k x}{\lambda}\right) \left[\frac{1 - \mathrm{e}^{-\frac{2\pi k t}{\lambda}}}{2} \frac{\lambda}{\pi k t} - 1\right]$$

The dipolar interlayer interaction pushing to reverse the DW is then

$$B_{\text{dip}}(x) = B_{\text{dip,S}}(x) + B_{\text{dip,V}}(x)$$

while the total dipolar field is finally

$$B_{\text{dip,t}}(x) = B_{\text{dip,S}}(x) + B_{\text{dip,V}}(x) + B_{\text{dip,self}}(x)$$

The DMI internal field along x of the Néel DW can be described by (*10*)

$$B_{\mathrm{dmi}}(x) = \frac{2D}{M_s}\frac{\partial m_z}{\partial x} = \frac{2D}{M_s\Delta}\,\mathrm{sech}^2\left(\frac{x}{\Delta}\right)$$

as we approximate it to a classical tan profile.

In order to compare the strengths of B_{dip} and B_{dmi}, we evaluate their actions locally by integration across the DW

$$\mathcal{A} = \frac{1}{6\Delta}\int_{-3\Delta}^{3\Delta} B(x)m_x(x)dx$$

that corresponds to the in-plane rotation driving force acting on the DW of the top layer.

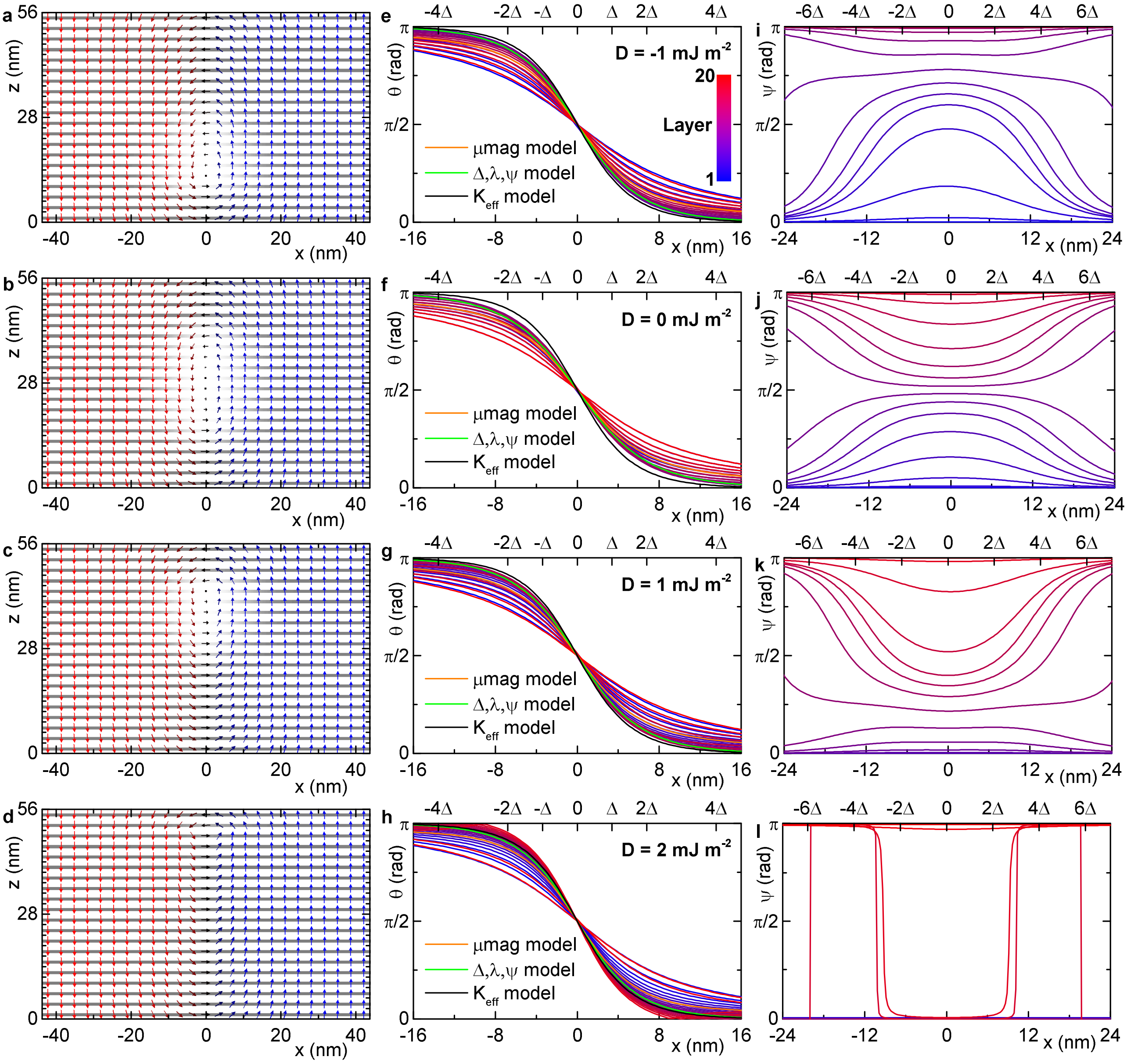

Fig. S1. Detailed version of Fig. 1. a–d. Cross-sectional view of a half simulation volume for $[\mathrm{X}(1)/\mathrm{Co}(0.8)/\mathrm{Z}(1)]_{20}$ multilayer with D = -1.0, 0.0, 1.0 and 2.0 mJ m^{-2}, respectively. Arrows point in the direction of the magnetisation, m_z is given by the colour of the arrows from red (-1) to blue (+1), while m_y is displayed by the colour of the grid from black (-1) to white (+1). e–h. Polar angle θ inside the DW in each layer for D = -1.0–2.0 mJ m^{-2}. The blue to red lines correspond to layers from bottom to top (see colour scale in e.), while the orange line is the average θ across the thickness. Green and black lines are the profiles as given by the (Δ,λ,ψ) and K_{eff} models, respectively. i–l. Azimuthal angle ψ inside the DW in each layer for D = -1.0–2.0 mJ m^{-2}. The blue to red lines again correspond to layers from bottom to top.

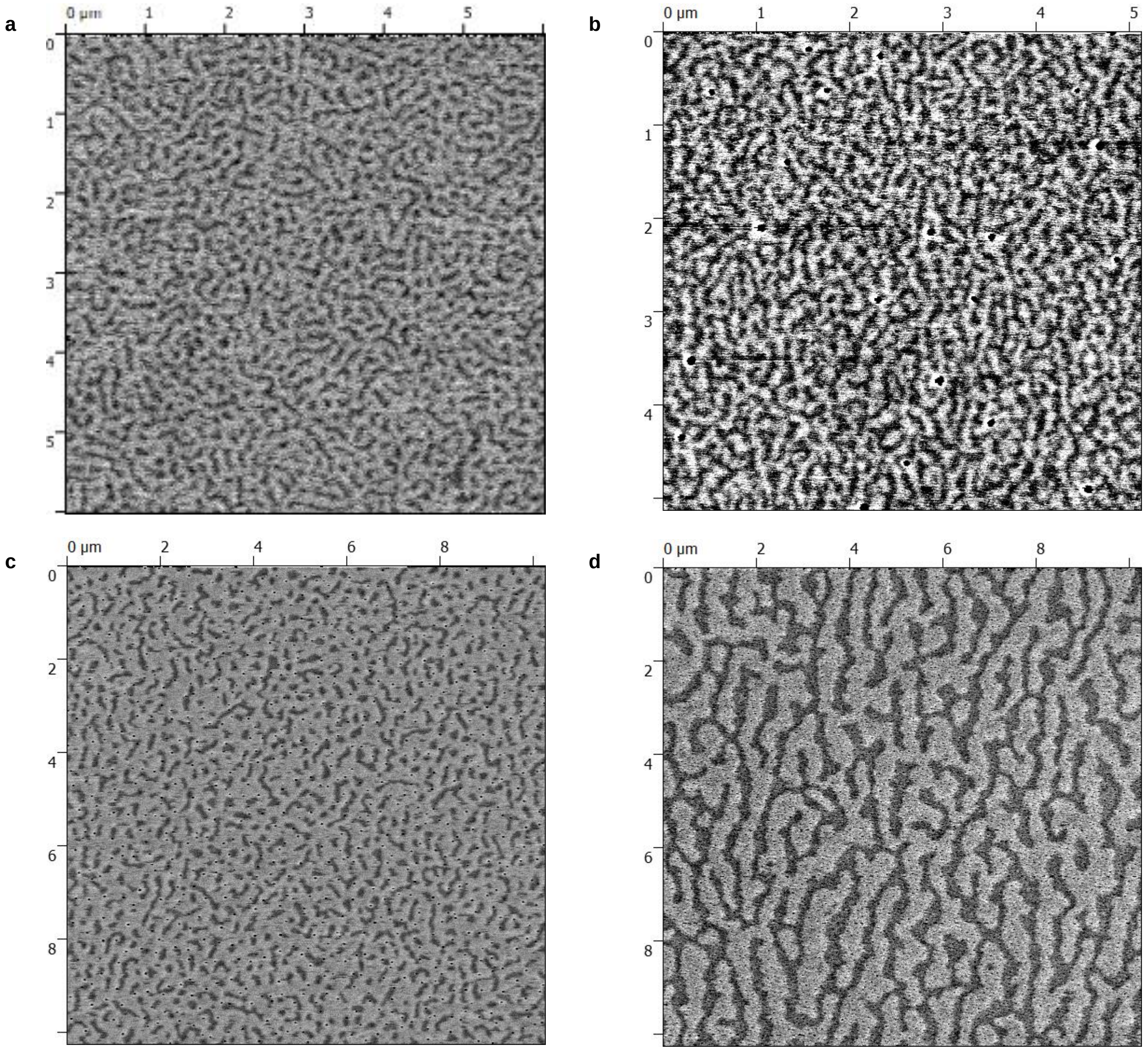
a
0 µm
1
2
3
4
5
0
1
2
3
4
5
b
0 µm
1
2
3
4
5
0
1
2
3
4
c
0 µm
2
4
6
8
0
2
4
6
8
d
0 µm
2
4
6
8
0
2
4
6
8

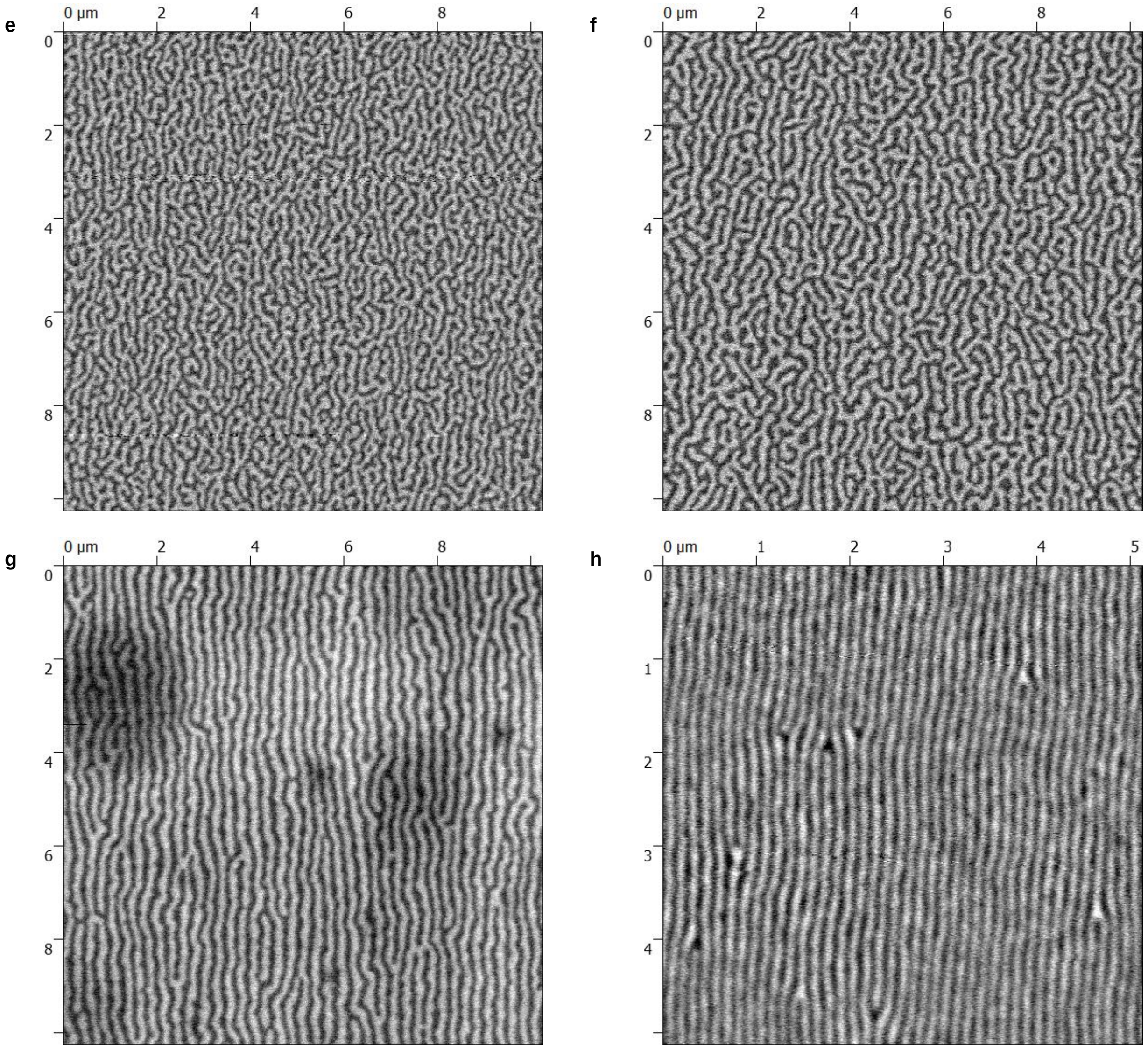
e
0 µm
2
4
6
8
0
2
4
6
8
f
0 µm
2
4
6
8
0
2
4
6
8
g
0 µm
2
4
6
8
0
2
4
6
8
h
0 µm
1
2
3
4
5
0
1
2
3
4

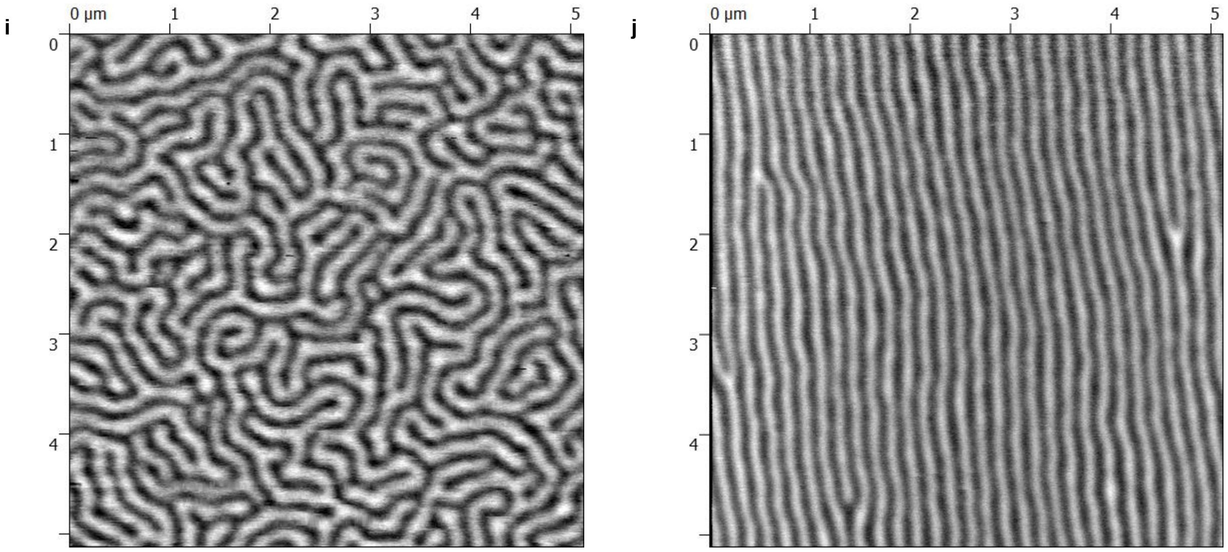

Fig. S2. MFM images of domain structures in studied multilayers. a–g. In-plane field demagnetised multilayers (I) to (VII). h. In-plane demagnetised multilayer (IX). i. Out-of-plane and j. in-plane demagnetised multilayer (VIII).